Sulfate attack mechanism and service life prediction of concrete under drying-wetting cycles synergistically regulated by hybrid fibers and CaO-MgO-based expansive agent

Case Studies in Construction Materials 25 (2026) e06462

Contents lists available at ScienceDirect

Case Studies in Construction Materials

journal homepage: www.elsevier.com/locate/cscm

Sulfate attack mechanism and service life prediction of concrete under drying-wetting cycles synergistically regulated by hybrid fibers and CaO-MgO-based expansive agent

Su Lu [a,b,1], Jiaxin Liu [a,b,2], Alessandro P. Fantilli [b,3], Xiao Sun [a,4], Lei Gan [a,c,f,5], Giuseppe Lacidogna [b,6], Jianqing Tang [a,b,7], Yunlin Ma [a,c,8], Tong Wang [a], Yang Lu [a,d,*,9], Zhenghong Tian [a,e,*,10]

[a] College of Water Conservancy & Hydropower Engineering, Hohai University, Nanjing 210098, China
[b] Department of Structural, Geotechnical and Building Engineering-DISEG, Politecnico di Torino, Corso Duca degli Abruzzi 24, Torino 10129, Italy
[c] National Key Laboratory of Water Disaster Prevention, Hohai University, Nanjing 210098, China
[d] International Joint Laboratory of Long-term Behaviour Environmentally Friendly Rehabilitation Technologies on Dams, Hohai University, Nanjing 210098, China
[e] Suzhou Research Institute of Hohai University, Suzhou 215100, China
[f] College of Water Conservancy and Civil Engineering, Xizang Agriculture and Animal Husbandry University, Nyingchi 860000, China

ARTICLE INFO

Keywords:
Fiber-reinforced concrete
CaO-MgO based expansive agent
Drying-wetting cycles
Sulfate attack
Parallel bar model
Service life prediction

ABSTRACT

To address the durability degradation of concrete exposed to sulfate-rich dry-wet environments, this study investigated the synergistic effects of modified polyester fibers (PF), basalt fibers (BF), and their hybrid system (PB) combined with a calcium-magnesium composite expansive agent (CMEA). Damage evolution during exposure to a 15% Na_2SO_4 solution was characterized in terms of, electrical response, phase assemblage, pore structure (PS), and microstructure. Layered damage and service-life prediction models were also developed. The mechanical performance (MP) and mass changes of the specimens exhibited three distinct stages: early enhancement, intermediate deterioration, and gradual late-stage degradation. The composite containing BF and 4% CMEA (BF-4E) exhibited the best overall durability, with a compressive strength retention ratio of 54.17% after 50 cycles. Although the composite containing PB and PB-4E provided a more balanced improvement in splitting tensile resistance and resistance to surface spalling. Its splitting

* Corresponding authors at: College of Water Conservancy & Hydropower Engineering, Hohai University, Nanjing 210098, China
E-mail addresses: lusu0821@hhu.edu.cn (S. Lu), ljx1104@hhu.edu.cn (J. Liu), alessandro.fantilli@polito.it (A.P. Fantilli), xiaos@hhu.edu.cn (X. Sun), ganlei2015@hhu.edu.cn (L. Gan), giuseppe.lacidogna@polito.it (G. Lacidogna), qing93@hhu.edu.cn (J. Tang), mayunlin@hhu.edu.cn (Y. Ma), 251302020038@hhu.edu.cn (T. Wang), luy@hhu.edu.cn (Y. Lu), zh-tian@hhu.edu.cn (Z. Tian).
[1] https://orcid.org/0009-0004-9691-3185
[2] https://orcid.org/0009-0005-1237-0011
[3] https://orcid.org/0000-0003-0383-7191
[4] https://orcid.org/0000-0001-5059-0158
[5] https://orcid.org/0000-0002-1722-4436
[6] https://orcid.org/0000-0002-0192-3793
[7] https://orcid.org/0009-0007-2313-9813
[8] https://orcid.org/0009-0008-5051-9122
[9] https://orcid.org/0000-0002-3336-7402
[10] https://orcid.org/0000-0001-7509-4644

https://doi.org/10.1016/j.cscm.2026.e06462
Received 21 June 2026; Received in revised form 5 August 2026; Accepted 23 August 2026
Available online 26 August 2026

tensile strength (STS) retention ratio was 72.60% after 40 cycles, while its mass loss (ML) rate was only 6.21% after50 cycles. Increasing the CMEA dosage to 8% intensified late-stage crack propagation due to excessive expansion and consequently reduced durability. The R^2 values of all developed models exceeded 0.96. At a critical damage depth of 30 mm, the model-predicted life of BF-4E under the adopted accelerated exposure conditions was 122 cycles, representing a 33.60% improvement over the reference mixture. These findings provide a basis for the mixture design and model-based durability assessment of fiber-CMEA reinforced concrete (FERC) exposed to sulfate environments.

1. Introduction

Concrete structures in sulfate-rich service environments, such as salt lakes, sulfate-bearing saline soils, and marine regions, are susceptible to sustained sulfate attack (SA) [1]. When SA is coupled with cyclic drying and wetting, moisture migration, ion transport, salt crystallization, and chemical reactions mutually reinforce one another, thereby accelerating material deterioration [2]. During drying, water evaporation progressively concentrates the pore solution and induces the precipitation of sulfate crystals. During rewetting, residual thenardite may dissolve and generate local supersaturation with respect to mirabilite. Crystal growth within confined pores can then produce crystallization pressure and contribute to cracking [3]. Meanwhile, the ingressing SO_4^{2-} reacts with cement hydration products to form sulfate-bearing crystalline phases, including ettringite (AFt) and gypsum. At the initial stage of exposure, continued hydration and the limited formation of reaction products can partially fill the available pore space [4]. As the cycles proceed, sulfate-bearing products continue to accumulate and interact with drying- and wetting-induced deformation, generating stresses in pore walls, promoting microcrack propagation, and increasing pore connectivity [5]. These changes eventually lead to mass loss (ML) and mechanical deterioration [6,7]. Moreover, pore-structure degradation under the coupled action of SA and dry-wet cycles (DWs) may precede a pronounced reduction in macroscopic strength. Material performance generally undergoes a stage-dependent transition from an early pore-filling effect to subsequent damage accumulation [8]. Therefore, retarding the evolution of microcracks from localized initiation to propagation, interconnection, and macroscopic cracking is critical for improving the resistance of cement-based materials to sulfate DWs.

Incorporating fibers into concrete is an effective physical reinforcement strategy for suppressing cracking induced by crystallization pressure and chemical expansion (CE). Fibers restrain the initiation and propagation of microcracks through crack bridging, pinning, and energy dissipation during interfacial pull-out, thereby improving the toughness and damage tolerance of the cementitious matrix. Recent studies have further shown that fiber reinforcement is jointly governed by fiber dosage, dispersion, and fiber-matrix interfacial characteristics. An appropriate fiber dosage can improve bond-mediated stress transfer and deformation capacity in damaged concrete, although the degree of reinforcement depends on both the fiber content and the damage state of the matrix [9,10]. At excessive dosages, fiber agglomeration and increased local porosity may weaken the reinforcing effect [11]. Because an individual fiber type is effective only over a limited range of crack scales and fiber contents, hybrid fibers (HF) with different mechanical properties (MP) provides a feasible approach to coordinating microcrack control, crack bridging, and energy dissipation. Previous studies have shown that high-modulus fibers primarily bridge cracks and restrain crack opening, whereas ductile polymer fibers dissipate energy mainly through deformation, interfacial sliding, and pull-out. The synergistic effect between these fiber types depends on their hybrid ratio and spatial distribution [12]. Other HF systems exhibit a similar dosage dependence. An appropriate hybrid ratio helps maintain the MP and interfacial bond capacity of concrete, whereas an excessive total fiber content may adversely affect performance because of poor dispersion and increased local defects [13]. Therefore, the reinforcing effect of HF is not a simple superposition of the contributions of individual fibers. Instead, it depends on the complementarity of their MP and their compatibility with the characteristic crack scales and damage evolution of the matrix.

During sulfate DWs, dispersed surface microcracks progressively propagate inward, widen, and interconnect. A single fiber type is therefore generally unable to meet the crack-control requirements associated with different damage stages and crack scales [14]. Modified polyester fibers (PF) have a relatively low elastic modulus (E), high ultimate elongation, and good alkali resistance, enabling them to form a flexible crack-control network with high deformation capacity within the matrix. Previous studies have shown that PF can suppress bleeding and excessive surface moisture migration during the fresh and early hardening stages, thereby reducing initial defects caused by moisture-loss shrinkage. During service, PF can alleviate stress concentration at crack tips through crack bridging, interfacial sliding, and pull-out energy dissipation, thus restraining the initiation and propagation of dispersed surface microcracks [15]. However, because PF has relatively low tensile strength (TS) and E, its capacity to restrain crack propagation and resist high crystallization-induced expansive stresses during the intermediate and later stages of SA is limited [15,16]. In contrast, basalt fibers (BF) have a higher E and TS. Their high strength and stiffness enable the formation of a stable crack-bridging framework that effectively transfers tensile stress across crack faces and restrains crack opening, widening, and interconnection [12,15]. Nevertheless, BF has a relatively low elongation and provides limited energy dissipation through deformation and pull-out [14,17]. Its relatively high density and unit cost also mean that increasing the BF dosage alone may raise material costs and impose more stringent requirements on fiber dispersion and interfacial quality [15].

Because PF and BF differ in stiffness, deformation capacity, and effective crack-control scale, their appropriate hybridization allows the flexible crack-arresting network formed by PF to interweave with the rigid bridging framework provided by BF. This produces a multiscale and stage-dependent crack-control system that combines flexibility with rigidity [14]. From the perspective of damage

evolution [14,15], PF is more effective in controlling dispersed microcracks at the early stage and dissipates energy through fiber deformation and interfacial sliding. BF provides stronger crack bridging and crack-opening restraint after cracks begin to propagate. In terms of the crack-control hierarchy [12,14,15], PF suppresses dispersed surface microcracks and initial transport pathways, thereby contributing to a surface crack-arresting effect. In contrast, the bridging and load-bearing actions of BF on propagating cracks help preserve the structural integrity of the inner matrix. Together, these effects establish a synergistic protection mechanism that combines a surface crack-arresting barrier with internal bridging reinforcement. This mechanism can weaken the mutually reinforcing relationship between crack propagation and aggressive-medium transport while mitigating interfacial damage caused by repeated drying- and wetting-induced deformation. Previous studies have shown that appropriately combining fibers with different stiffnesses and deformation capacities can provide mechanical and durability performance comparable to that of systems containing only high-modulus fibers while reducing the required amount of high-modulus fibers [14,15]. In the PF-BF system, the partial replacement of BF with lower-density and lower-cost PF not only exploits the complementary crack-control scales of the two fibers but also reduces BF consumption. This can lower the cost and embodied carbon associated with fiber use and improve both the performance and resource efficiency of the fiber-reinforced system. However, fibers primarily regulate crack evolution through mechanical mechanisms and cannot directly prevent SO_4^{2-} transport through capillary pores and interfacial defects. Their effect on pore connectivity also depends on fiber dosage, dispersion, and fiber-matrix interfacial quality [18]. In addition, fibers cannot directly compensate for the volumetric shrinkage of the cementitious matrix [15,19]. When fibers are unevenly distributed or insufficiently bonded to the matrix, pores and interfacial defects around the fibers may provide additional pathways for aggressive-medium transport [20]. Therefore, hybrid-fiber crack control alone cannot simultaneously achieve crack restraint, shrinkage compensation, and pore-structure densification.

To improve the volumetric stability of the matrix and reduce pore connectivity, chemical volume compensation using an expansive agent (EA) can serve as an effective complement to fiber reinforcement. The expansion development of a single CaO or MgO based EA is governed by its hydration kinetics and may not fully match the shrinkage evolution of cement-based materials at different stages [21,22]. A calcium-magnesium composite EA (CMEA) combines CaO and MgO components with different hydration rates, thereby providing volume compensation over different time periods [22]. CaO hydrates relatively rapidly to form $Ca(OH)_2$, providing early-age volume compensation and partially filling the pore space [23]. In contrast, MgO hydrates more slowly, and the gradual formation of $Mg(OH)_2$ extends the duration of volume compensation [24]. At an appropriate dosage, these hydration products can mitigate matrix shrinkage, improve interfacial contact, and refine the local pore structure (PS). $Ca(OH)_2$ can also help maintain pore-solution alkalinity. However, under sulfate exposure, it may also provide a calcium source for the formation of sulfate-bearing phases such as gypsum [15]. In addition, some CMEA formulations contain sulfate-bearing components that regulate hydration and expansion. Increasing the CMEA dosage may therefore increase both the content of expansive constituents and the initial internal inventory of sulfate-bearing components [15,21,22]. Consequently, the role of CMEA under sulfate exposure cannot be attributed solely to volume compensation or pore filling. Instead, it depends on the dynamic balance among hydration-induced expansion, pore-structure evolution, and sulfate-bearing phase formation. For fiber-CMEA composite systems, whether this balance produces a stable structural benefit further depends on the compatibility between the degree of CMEA-induced expansion and the restraining capacity of the fiber network.

In fiber-CMEA composite systems, CMEA hydration produces $Ca(OH)_2$ and $Mg(OH)_2$ together with moderate volumetric expansion. These hydration products can fill part of the capillary pore space and interfacial defects, mitigate matrix shrinkage, and improve local microstructural continuity [15,25,26]. When the expansive deformation is restrained by fiber-matrix bonding and the distributed constraint provided by the fiber network, part of the free expansion is converted into restrained expansion. This process generates a certain degree of internal compressive prestress, which counteracts part of the tensile stress induced by subsequent shrinkage and delays microcrack initiation [15,26]. Meanwhile, PF and BF provide complementary crack-control mechanisms, including microscale crack bridging, restraint across propagating cracks, crack deflection, and pull-out energy dissipation. These mechanisms restrain the evolution of cracks from initiation to widening and interconnection [15,25]. The denser matrix and interfacial structure resulting from pore filling and shrinkage compensation, in turn, help maintain fiber bonding and stress transfer. Fibers and CMEA therefore produce a synergistic reinforcing effect through shrinkage compensation, restrained-expansion regulation, pore filling, and crack bridging [19,27]. Previous studies have shown that the combined use of fibers and EA generally provides greater improvements in shrinkage control, cracking resistance, and impermeability than either component used alone. This improvement arises because reduced pore connectivity and controlled crack widths jointly restrict the transport pathways for moisture and aggressive ions [15,19,27]. However, this synergistic effect depends on the CMEA dosage, fiber stiffness and content, fiber dispersion, interfacial bonding, and curing conditions. Improvements in volumetric stability, crack control, and durability can be achieved simultaneously only when the degree of expansion is compatible with the restraining capacity of the fiber network.

Existing studies have focused mainly on the shrinkage compensation [15,25,26], early-age cracking resistance, and impermeability [19,27] of fiber-expansive-agent composite systems under conventional environmental conditions. However, their long-term synergistic effects under sulfate DWs remain insufficiently understood. In this environment, external SO_4^{2-} transport and salt crystallization may occur simultaneously with the continued hydration of CaO and MgO in CMEA and the involvement of internal sulfate-bearing components in phase evolution. These processes couple pore filling, restrained expansion, sulfate-bearing phase accumulation, and crack propagation. In particular, quantitative evidence is still lacking regarding how the CMEA dosage governs the transition from early pore filling to later expansion-induced deterioration and how different fiber systems regulate this transition. Establishing these mechanisms requires correlating phase assemblage, PS, electrical response, and macroscopic performance [14,15,19,28,29]. Moreover, existing durability assessments have focused primarily on macroscopic indicators such as mass and strength. Few studies have systematically considered the nonuniform damage caused by sulfate ingress along the penetration depth or the influence of such

layered deterioration on the overall load-bearing capacity and service life [30–32].

Accordingly, this study systematically investigated the effects of PF, BF, their hybrid system (PB), and different CMEA dosages on the performance of concrete under sulfate DWs. MP, SO_4^{2-} penetration depth (PD), mass changes, and electrical resistivity (ER) were measured to characterize macroscopic deterioration, sulfate transport, and electrical response. Electrochemical impedance spectroscopy (EIS), X-ray diffraction (XRD), and Fourier-transform infrared spectroscopy (FTIR) were used to analyze conductive pathways, the relative distribution of crystalline phases, and the main chemical bonding characteristics. Mercury intrusion porosimetry (MIP) and scanning electron microscopy (SEM) were further employed to reveal the evolution of PS and microstructural morphology. Based on the combined macroscopic, electrical, phase, pore-structure, and microstructural results, the synergistic mechanisms by which fibers and CMEA regulate sulfate dry-wet damage in fiber-CMEA reinforced concrete (FERC) were clarified. Finally, a layered damage mechanics model accounting for nonuniform deterioration along the sulfate penetration depth was developed using a non-steady-state diffusion equation and a parallel-bar system. The model was then used to estimate the sulfate resistance life of FERC. This study provides a theoretical basis for fiber selection, CMEA dosage design, and model-based service-life assessment of fiber-expansive-agent cementitious composites exposed to complex sulfate environments.

2. Methodology

2.1. Materials and specimen preparation

2.1.1. Raw materials

P·O 42.5 R ordinary Portland cement (OPC), manufactured by Nanjing Conch Cement Co., Ltd., was used as the primary binder. Class II fly ash (FA), supplied by Jiangsu Tongyu New Materials Technology Co., Ltd., was incorporated to optimize particle packing and improve durability. A CMEA, produced by Jiangsu Sobute New Materials Co., Ltd., was introduced to mitigate shrinkage-induced cracking. The chemical compositions of these powder materials are listed in Table 1, while their physical properties are presented in Tables 2 and 6. Their phase compositions, surface morphologies, and particle-size distributions are shown in Figs. 1–3, respectively. Limestone manufactured sand with a fineness modulus of 2.8 and a particle-size range of 0–5 mm was used as the fine aggregate (FTG). Natural crushed stone was used as the coarse aggregate (CA). Based on the dense-packing principle, the 10–25 mm and 5–10 mm fractions were blended at a mass ratio of 7:3 to obtain a continuous particle-size distribution of 5–25 mm. The physical properties of the aggregates are provided in Tables 3 and 4. Chopped BF and monofilament PF were used as reinforcing materials. BF was supplied by Changsha Ningxiang Building Materials Co., Ltd., while PF was manufactured by Hebei Defeng PF Co., Ltd. Their MP and macroscopic morphologies are presented in Table 5 and Fig. 4, respectively. To ensure adequate workability, a PCA-I type polycarboxylate-based superplasticizer (SP), produced by Jiangsu Sobute New Materials Co., Ltd., was added to the mixtures. Its water-reduction rate was 26.5%.Table 6

2.1.2. Mix proportions

C40-grade concrete was adopted as the reference system. Based on relevant mix-design standards and preliminary workability tests [33], the water-to-binder ratio (W/B) was fixed at 0.43. The fiber dosages used in this study were selected according to the results of systematic screening conducted in previous work [14]. Four fiber volume fractions of 0.05%, 0.10%, 0.15%, and 0.20% were investigated in a comparable C40 concrete system, with workability, MP, and durability under sulfate DWs evaluated comprehensively. Within the investigated ranges, the best-performing volume fractions of PF, BF, and HF (PB) were 0.10%, 0.15%, and 0.15% [14], respectively. Accordingly, 0.10% PF and 0.15% BF were selected as the single-fiber dosage levels. The total fiber volume fraction of PB was fixed at 0.15%, comprising 0.075% PF and 0.075% BF at a PF-to-BF volume ratio of 1:1. The CMEA dosages were determined based on preliminary tests and a previously published study. Within the material system investigated, 4% CMEA provided effective shrinkage compensation and pore filling while allowing the fiber network to restrain expansion. When the dosage increased to 8%, excessive expansive products and internal volumetric deformation could induce microcracking and reduce mechanical performance [15]. Therefore, CMEA dosages of 0%, 4%, and 8% were selected. The 0% dosage served as the baseline, 4% represented the suitable dosage identified in the previous study, and 8% served as a high-dosage comparison to examine the transition from beneficial volume compensation and pore filling to detrimental expansion-induced damage.

The CMEA dosage was expressed as a percentage of the total mass of cementitious materials. CMEA was introduced through equal-mass and proportional replacement of cement and fly ash. The CMEA contents at the 4% and 8% dosage levels were 17.2 and 34.4 kg/m^3, respectively, with the cement and fly ash contents reduced proportionally. Consequently, the total cementitious material content, water content, and W/B of all mixtures were maintained at 430 kg/m^3, 184.9 kg/m^3, and 0.43, respectively. The detailed mix proportions are presented in Table 7.

Table 1
Major chemical compositions of OPC, FA, and CMEA (wt%).

Types	CaO	Fe_2O_3	Al_2O_3	MgO	SiO_2	K_2O	P_2O_5	SO_3	Na_2O	TiO_2	MnO
OPC	63.87	3.81	5.06	1.08	20.85	0.97	0.21	2.33	0.16	0.32	0.30
FA	6.60	5.94	18.93	3.67	55.98	1.95	0.16	1.90	0.50	0.15	0.12
CMEA	44.32	3.86	3.19	29.57	2.65	0.32	0.15	14.07	0.71	0.12	-

Table 2
Main properties of OPC and FA.

Types	Specific surface area (m^2/kg)	Fineness (%)	Density(g/cm^3)	Flexural strength (MPa)		Compressive strength (CS) (MPa)	
				3d	28d	3d	28d
OPC	366	2.1	3.10	4.77	8.42	25.26	50.18
FA	343	4.6	2.32	-	-	-	-

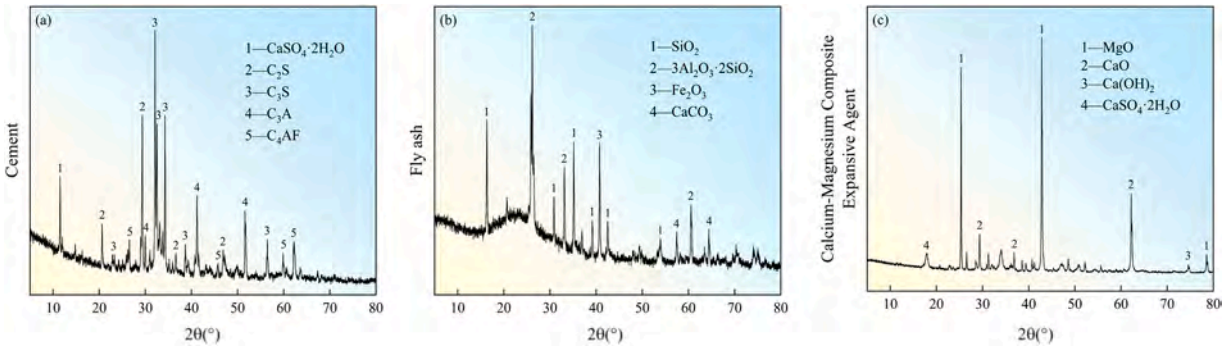

Fig. 1. Phase compositions of OPC, FA, and CMEA.

Fig. 2. Surface morphologies of OPC, FA, and CMEA particles.

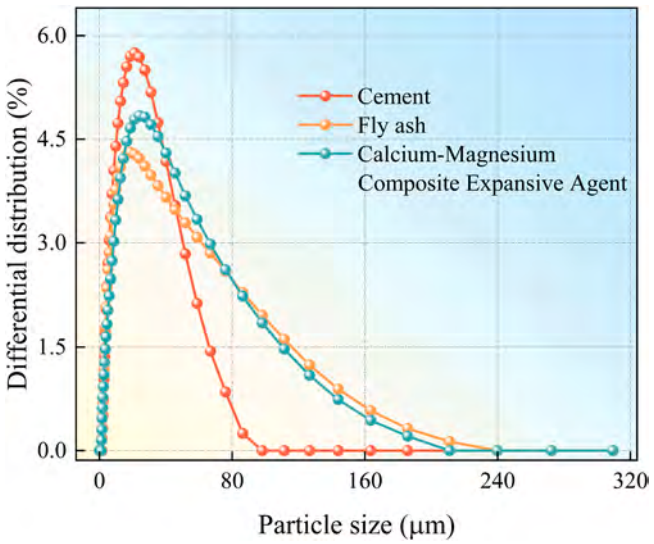

Fig. 3. Particle size distributions of OPC, FA, and CMEA.

Table 3
Main properties of FAG.

Apparent density (kg/m^3)	Sediment percentage (%)	Moisture content (%)	Stacking density (kg/m^3)		Fineness modulus	Particle size gradation (mm)	Mud content (%)	Stone powder content (%)
			Dense	Loose				
2690	0.7	2.8	1710	1576	2.8	0–5	0.8	8

Table 4
Main properties of CA.

Sediment percentage (%)	water absorption (%)	Needle flake stone (%)	Stacking density (kg/m^3)		Particle size gradation (mm)	Apparent density (kg/m^3)	Crushing index (%)	Mud content (%)
			Dense	Loose				
0.5	0.6	3.8	1680	1556	5–25	2750	5.8	0

Table 5
Main properties of fibers.

Types	TS (MPa)	Alkali resistance (Strength retention rate, %)	Length (mm)	*E* (GPa)	Diameter (μm)	Melting point (℃)	Density (g/cm^3)	Elongation (%)
PF	1861	96.3	12	26.6	28.22	265	1.31	13
BF	1556	86	12	95.6	17	1050	2.65	3

2.1.3. Mixing procedure of FERC

The preparation procedure, detailed in Fig. 5, commenced with a 3 min dry-mixing of fibers, FAG, and binders to achieve an optimal dispersion state. Subsequent to a brief 30-s blending with CA, the remaining water and SP were added, followed by a 1.5 min intensive wet-mixing phase to ensure matrix homogeneity. Post-casting, the samples were compacted through vibration and maintained in their molds for 24 h. After demolding, the specimens were transferred to a regulated environment for standardized curing until the designated experimental periods.

2.2. Experimental program and test methods

2.2.1. Sulfate DWs test

The sulfate DWs test was based on the 24 h cycling framework specified in GB/T 50082–2009 [34], with adjustments made according to previous studies on BF -reinforced concrete and the preliminary test protocol developed by the research group [14,35,36]. Previous research compared the performance evolution of basalt-fiber-reinforced concrete exposed to 7% and 15% Na_2SO_4 solutions.

Fig. 4. Appearance of fibers.

Table 6
Main properties of CMEA.

Fineness (%)	Specific surface area (m^2/kg)	CS (MPa)		Restricted expansion rate		Setting time (min)	
		7d	28d	Water (7d)	Water (21d)	Initial	Final
0.27	375	33.7	47.2	0.051	-0.014	200	340

Table 7
FERC mix (kg/m^3).

	Water	OPC	FA	CA	FAG	SP	PF (vol%)	BF (vol%)	CMEA
CO	184.9	355	75	1024.75	772.7	5.16	-	-	-
CO-4E		340.8	72						17.2
CO-8E		326.6	69						34.4
PF		355	75				0.1	-	-
PF-4E		340.8	72						17.2
PF-8E		326.6	69						34.4
BF		355	75				-	0.15	-
BF-4E		340.8	72						17.2
BF-8E		326.6	69						34.4
PB		355	75				0.075	0.075	-
PB-4E		340.8	72						17.2
PB-8E		326.6	69						34.4

Note: CO denotes the reference mixture without fibers or CMEA. PF, BF, and PB represent the mixtures containing PF alone, BF alone, and their hybrid combination, respectively. The PF and BF dosages were calculated as volume fractions of concrete. The total fiber volume fraction of PB was 0.15%, comprising 0.075% PF and 0.075% BF at a PF-to-BF volume ratio of 1:1. The suffixes "-4E" and "-8E" indicate the mass replacement ratios of CMEA. For example, PB-8E denotes the mixture containing HF at a total volume fraction of 0.15% and CMEA at a mass replacement ratio of 8%.

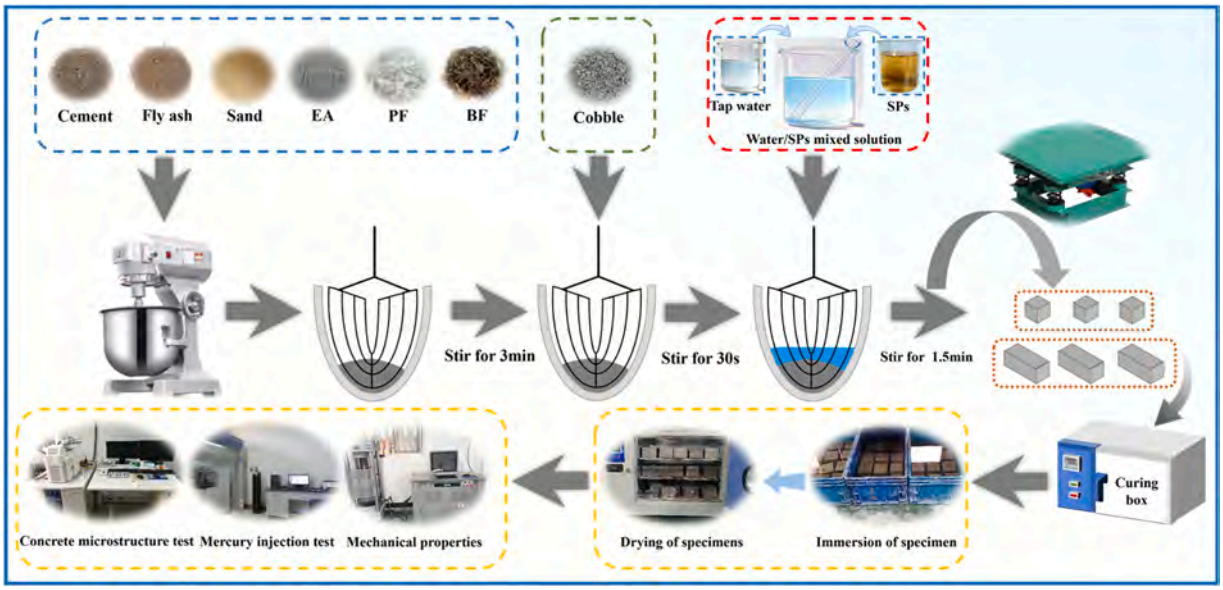

Fig. 5. Preparation process and test contents of FERC specimens.

At a concentration of 7%, the specimen strength generally continued to increase over 50 cycles. In contrast, exposure to the 15% solution produced a stage-dependent transition from early strength enhancement to subsequent deterioration [35,36]. Therefore, a 15% Na_2SO_4 solution by mass was adopted in this study to produce distinguishable deterioration within a limited number of cycles and to compare the relative durability of different fiber-CMEA systems. A drying temperature of 60℃, verified through preliminary tests by the research group, was selected [14,35,36]. This temperature promoted pore-water evaporation and sulfate-solution concentration while reducing the potential additional thermal disturbance to cement hydration products and the concrete microstructure associated with higher drying temperatures.

Cubic specimens measuring 100 mm× 100 mm× 100 mm were used. After standard curing for 26d, surface moisture was removed, and the specimens were predried in a forced-air oven at 60℃ for 48 h to standardize their initial moisture states before sulfate exposure. The specimens were then cooled to room temperature, and their initial masses were measured. Each DWs lasted 24 h and consisted of immersion in the 15% Na_2SO_4 solution for 15 h, air drying at room temperature for 1 h, oven drying at 60℃ for 6 h, and cooling at room temperature for 2 h. To minimize the effect of concentration changes in the exposure solution during cycling, the Na_2SO_4 solution was renewed every 10 cycles, and its pH was monitored and recorded. A total of 50 DWs were conducted.

2.2.2. MP after SA

MP were evaluated after 0, 10, 20, 30, 40, and 50 sulfate DWs in accordance with GB/T 50081–2019 [37] and GB/T 50082–2009 [34]. Three specimens were tested for each condition. CS and splitting tensile strength (STS) were measured using a hydraulic testing

machine under loading rates of 0.6 MPa/s and 0.06 MPa/s, respectively. The strength retention ratio was defined as:

$$K = \frac{f_n}{f_0} \times 100\% \tag{1}$$

where $K_c$and $K_t$denote the retention ratios of CS and STS after n DWs, respectively (%); $f_{cn}$and f_{tn} represent the measured CS and STS after n DWs (MPa); and $f_{c0}$and f_{t0} correspond to the strengths of non-deteriorated reference concrete (MPa).

2.2.3. SO_4^{2-} PD analysis

(1) Test procedure for SO_4^{2-} PD

The spatial distribution of SO_4^{2-} concentration was quantitatively determined using the barium sulfate gravimetric technique [14], adhering to the analytical protocols established in GB/T 50476–2019 [38] and GB/T 11899–89 [39]. Specimens were ground layer-by-layer, and the collected powders were dissolved in dilute HCl. After filtration, $BaCl_2$ was added to precipitate $BaSO_4$, followed by drying to constant mass for quantification. The entire testing procedure is illustrated in Fig. 6. The sulfate mass fraction within the FERC matrix was computed using Eq. (2):

$$\omega_{SO_4^{2-}} = \frac{0.4116 \times m}{M} \times 100\% \tag{2}$$

where $\omega_{SO_4^{2-}}$ denotes the sulfate mass fraction (%); 0.4116 represents the gravimetric factor derived from the molar mass ratio of SO_4^{2-}; m is the mass of the generated $BaSO_4$ precipitate (g); and M corresponds to the initial mass of the powdered sample aliquot (g)

(2) Migration and evolution model of SO_4^{2-}

To quantitatively describe the diffusion distribution of SO_4^{2-} in FERC and to accurately predict the evolution of the erosion front, a modified prediction model based on Fick's law was established in this study. The experimentally measured SO_4^{2-} concentration profiles at different erosion stages were fitted using Fick's second law [40]. Under the assumptions of a semi-infinite medium and constant boundary conditions, the analytical expression is given by:

$$c(x,t) = c_i + (c_s - c_i) \bullet erfc\left(\frac{x}{2\sqrt{D_S \bullet t}}\right) \tag{3}$$

where $c(x,t)$ is the SO_4^{2-} concentration at depth x and exposure time t; c_s is the SO_4^{2-} concentration at the exposed surface; c_i is the initial SO_4^{2-} concentration; D_s denotes the apparent diffusion coefficient of SO_4^{2-} within the FERC; and *erfc* denotes the complementary error function.

Due to limitations in sampling precision, direct experimental measurements may exhibit sampling and measurement scatter. By performing nonlinear fitting based on Eq. (3), key durability parameters such as D_s can be extracted, and the physical diffusion depth of SO_4^{2-} can be more accurately determined.

Concerning the advancement of the erosion front depth d with time t under DWs, conventional steady-state diffusion analysis typically follows the square-root law, derived from Fick's first law [41], which assumes a linear relationship between flux J and concentration gradient:

$$J = -D_S \bullet \frac{\partial C}{\partial x} \tag{4}$$

$$d = k \bullet \sqrt{t} \tag{5}$$

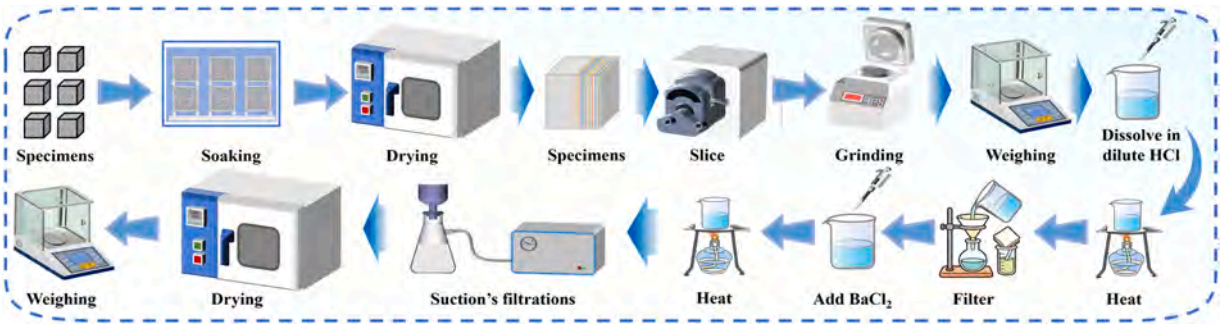

Fig. 6. Flow chart of the SO_4^{2-} PD test procedure.

where J is the diffusion flux of SO_4^{2-}; D_s is the diffusion coefficient; $\frac{\partial C}{\partial x}$ denotes the spatial concentration gradient; d is the PD in a porous material; and k is a material-dependent coefficient.

However, SA is a complex process involving the coupling of diffusion, chemical reactions, and expansion-induced damage [42]. The formation of erosion products dynamically alters the PS, leading to time-dependent changes in transport properties. This feedback mechanism violates the fundamental assumption of constant transport properties in classical Fickian diffusion.

To address this limitation, a time-dependent power-law model incorporating environment-material coupling effects was introduced to characterize the evolution of the erosion front:

$$d_s = k_p \bullet t^{\alpha} \tag{6}$$

where d_s is the SO_4^{2-} PD in FERC (mm); k_p is a permeability-related coefficient associated with material properties; and α is an exponent reflecting the influence of external environmental conditions.

2.2.4. ML evaluation

The ML ratio was employed to evaluate the physical spalling behavior of the matrix during SA [14]. A TC10K-HB high-precision electronic balance, manufactured by Changshu Shuangjie Testing Instrument Co., Ltd., was used, with a measuring range of 10 kg and an accuracy of 0.1 g. The specimens were weighed after 0, 10, 20, 30, 40, and 50 drying–wetting cycles.

The cumulative ML ratio $K_m$after n DWs was calculated as follows:

$$K_m = \frac{m_0 - m_n}{m_0} \times 100\% \tag{7}$$

where K_m is the ML ratio after n DWs (%); m_0 is the initial mass of the specimen before exposure (g); and m_n is the mass after n DWs (g). To ensure reliability and statistical significance, the final result for each mixture was taken as the arithmetic mean of three independent specimens.

2.2.5. Electrical properties characterization

Because the electrical resistivity (ER) and electrochemical impedance spectroscopy (EIS) responses of concrete are sensitive to the moisture state, pore-solution composition, and test temperature [43], all electrical measurements were performed immediately after the prescribed drying and cooling stages. For the specimens at 0 cycles, the initial measurements were conducted after predrying at 60℃ for 48 h and cooling to room temperature. At 10, 30, and 50 cycles, the measurements were conducted after oven drying at 60℃ for 6 h, followed by cooling at room temperature for 2 h. The cooling and testing temperatures were maintained at 20 ± 2℃. Before testing, the specimens were not subjected to any additional immersion, rinsing, or drying, and both the specimen surfaces and exposed electrode terminals were kept dry. ER measurements were followed immediately by EIS measurements using the same specimen sequence. After testing, the specimens were returned to the drying-wetting cycle procedure.

(1) **ER measurement**

Fig. 7(a) illustrates the experimental setup for ER measurement. The embedded two-electrode method was employed to determine the ER of the specimens [15,43,44]. Cubic specimens measuring 100 mm per side were prepared with two symmetrically positioned stainless steel mesh electrodes (120 mm × 99 mm × 1 mm) cast in situ. Electrode boundaries and protruding sections were insulated via epoxy encapsulation, whereas the four lateral faces remained uncoated to permit multidirectional ionic ingress during subsequent exposure regimes.

ER was measured using a TH2810B + digital inductance–capacitance–resistance (LCR) meter (Tonghui Electronics Co., Ltd., Changzhou, China) at an alternating-current (AC) frequency of 1 kHz. Each measurement was completed within 1 min. Three replicate specimens were tested for each mixture, and the mean value was reported.

The ER ρ was calculated as:

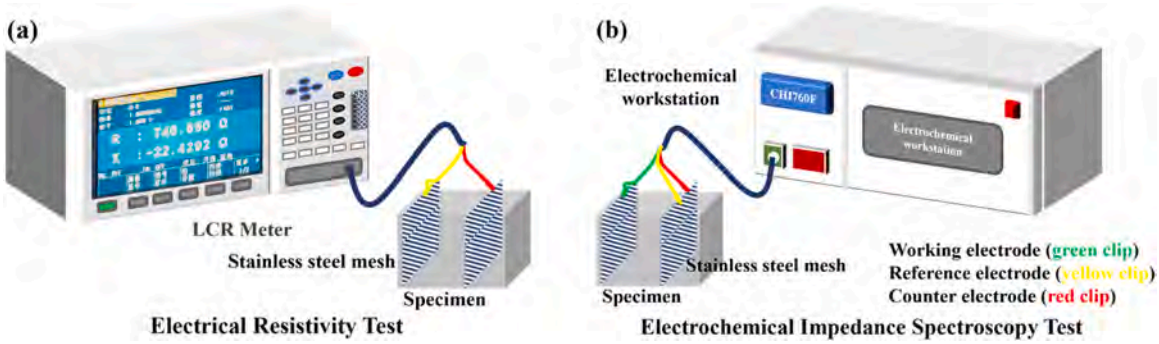

Fig. 7. Electrical response testing of FERC.

$$\rho = R\frac{A}{L} \tag{8}$$

where ρ denotes the bulk ER (Ω·m); R represents the recorded resistance (Ω); A corresponds to the effective cross-sectional area traversed by the current (m^2); and L signifies the inter-electrode spacing (m).

(2) **EIS monitoring**

EIS measurements were conducted using a CHI760F electrochemical workstation manufactured by Shanghai Chenhua Instruments Co., Ltd. A two-electrode system was adopted, as illustrated in Fig. 7(b) [43,44]. The working electrode (WE) was electrically coupled to one embedded stainless steel mesh, whereas the counter electrode and reference electrode (RE) were jointly connected to the opposing mesh. EIS tests were performed in situ at selected DWs (0, 10, 30, and 50 DWs). After each measurement, the specimens were immediately returned to the sulfate exposure system. A logarithmic frequency sweep was applied over a range of 10^{-2} to 10^5Hz. The minimum current range in the high-frequency region was set to 2 mA. A small-amplitude AC perturbation was used to maintain system equilibrium, and shielded cables with alligator clips were employed throughout the measurements.

2.2.6. XRD and FTIR analyses

To determine the crystalline phase assemblage and major chemical bonding characteristics of the specimens after sulfate DWs, concrete specimens subjected to 50cycles were selected for XRD and FTIR analyses. After the specimens were fractured, representative fragments were collected from the interior near the specimen center to minimize interference from residual exposure solution and precipitated sulfate salts on the specimen surfaces. The fragments were then immersed in anhydrous ethanol for 7d to stop further hydration, with the ethanol replaced three times during immersion. After immersion, the samples were dried to a constant mass in a forced-air oven at 45℃, thoroughly ground, and passed through a 200-mesh sieve. The resulting powder samples were sealed in resealable bags until XRD and FTIR testing.

(1) **XRD analysis**

The crystalline phase assemblage of the specimens after sulfate DWs was analyzed using a Rigaku Ultima IV X-ray diffractometer (Rigaku Corporation, Japan). Cu Kα radiation with a wavelength of λ= 1.54 Å was used. The tube voltage and current were set to 40 kV and 40 mA, respectively. The prepared powder was uniformly placed in the sample holder and gently pressed to produce a flat surface, thereby minimizing the effects of surface unevenness and preferred particle orientation on the diffraction results. The scanning range was 5°–90°, with a scanning rate of 4°/min and a step size of 0.02° in step-scanning mode.

The XRD patterns were processed using MDI Jade 9 software developed by Materials Data, Inc. Phase identification was performed using the International Center for Diffraction Data (ICDD) PDF-4 + 2009 powder diffraction database. The crystal-structure information of the corresponding phases was retrieved using FindIt software. After the major crystalline phases had been identified, the diffraction patterns were fitted, and the semi-quantitative analysis function of the software was used to compare the relative distributions of crystalline products among the specimens. The semi-quantitative results for four selected crystalline phases, AFt, $CaSO_4{\cdot}2\,H_2O$, $Ca(OH)_2$, and $Mg(OH)_2$, were further normalized so that their combined relative proportion was equal to 100%.

(2) **FTIR analysis**

Changes in the major chemical bonds and structural groups were analyzed using a Nicolet iS50 Fourier-transform infrared spectrometer (Thermo Fisher Scientific, USA). Samples were prepared using the KBr pellet method. Approximately 1 mg of powder passing through the 200-mesh sieve was mixed with approximately 100 mg of spectroscopic-grade KBr at a mass ratio of 1:100. The mixture was thoroughly ground and homogenized in an agate mortar and then pressed into a transparent pellet. Before testing, a background spectrum was collected using a pure KBr pellet. The spectra were recorded over the range of 4000–400 cm^{-1} at a resolution of 4 cm^{-1}.

2.2.7. Pore-structure and microstructural morphology analyses

(1) **PS characterization**

PS distributions were acquired via MIP employing an AutoPore IV 9500 automated analyzer. Upon termination of the designated DWs regime, specimens were fragmented into discrete pieces and subsequently immersed in isopropanol for 7d. This solvent exchange procedure served the dual purpose of arresting ongoing hydration reactions and effecting solvent exchange followed by drying. The fragments were thereafter transferred to a vacuum drying oven and held at 60 ℃ for 24 h to attain constant mass. To quantitatively characterize the evolution of PS during SA, a fractal dimension (D) based on a thermodynamic model was introduced, following established methods reported in the literature. The calculation procedure of the D is given by Eqs. (9)-(11)[15,45]:

$$D = \frac{\lg\left(\frac{W_n}{r_n^2}\right)}{\lg Q_n} \tag{9}$$

$$W_n = \sum_{i=1}^{n} \overline{P_i} \Delta V \tag{10}$$

$$Q_n = \frac{V_n^{1/3}}{r_n} \tag{11}$$

where D is the fractal (box-counting) dimension; r corresponds to the maximum pore radius accessed; i indexes the applied pressure increment; P_i denotes the mean pressure prevailing during the i-th intrusion step; ΔV represents the incremental volume of mercury intruded at that step; n indicates the total number of intrusion increments; r_n defines the pore radius associated with the n-th intrusion event; and V_n is the cumulative intruded mercury volume up to the n-th increment.

(2) **Microstructural observation**

The microstructural morphology of SA FERC was characterized using a Hitachi SU5000 high-resolution SEM. Samples were extracted from regions adjacent to the exposed surface in order to capture the morphology of corrosion products and their enrichment characteristics within the fiber-matrix fiber–matrix interfacial transition zone (ITZ). Prior to SEM observation, all specimens were coated with a thin gold layer to enhance electrical conductivity and ensure high-quality imaging.

3. Experimental results

3.1. MP after SA

3.1.1. CS

Fig. 8 illustrates the variation in CS and the corresponding retention ratio of all FERC subjected to SA under DWs. A characteristic three-stage evolution is observed, including an initial strengthening phase, a subsequent rapid degradation stage, and a final stabilization period. At the early exposure stage (0–10 DWs), all mixtures exhibit a noticeable increase in CS. For instance, the CO group increases from 43.13 MPa to 48.92 MPa, corresponding to a 13.42% enhancement. This behavior is mainly associated with the initial pore-refinement effect induced by sulfate ingress [46]. Specifically, infiltrated SO_4^{2-} reacts with hydration products to generate limited quantities of gypsum and AFt, which preferentially fill capillary pores and temporarily enhance matrix compactness and load-bearing capacity. With further exposure (10–40 DWs), a pronounced deterioration stage emerges. The continuous generation of expansive phases, combined with $Na_2SO_4{\cdot}10\ H_2O$ crystallization, induces progressive accumulation of internal stress within the PS [14]. Once the generated internal crystallization pressure surpasses the matrix's inherent tensile capacity, the onset of microcrack initiation and coalescence occurs. This is manifested by the nucleation and subsequent coalescence of microcracks, further exacerbated by the loss of adhesive integrity at the ITZ between aggregates and the cementitious paste. Consequently, a pronounced degradation in compressive strength is observed. Specifically, by the 30th DW cycle, the CS of the CO group recedes to 26.18 MPa, representing a retention ratio of merely 60.70%. The presence of fibers effectively delays this degradation process. In mono-fiber systems, BF, due to their higher E, exhibit superior crack-bridging and stress-transfer capabilities compared with PF, particularly in restraining macrocrack propagation [47]. The HF (PB) further enhances performance through rigid-flexible coupling, enabling coordinated control of microcrack initiation and macro-scale fracture resistance [48]. At 50 DWs, the BF group retains 46.18% of its initial CS, demonstrating significantly

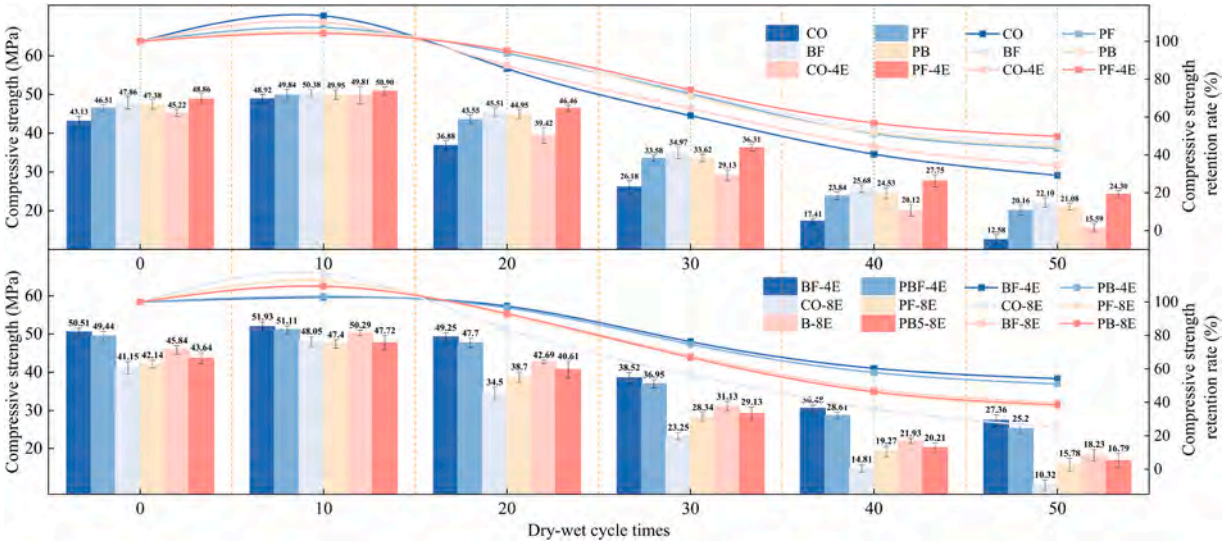

Fig. 8. CS and corresponding retention ratios of FERC with different mix proportions under sulfate DWs.

improved mechanical stability relative to the control group.

Further improvement is achieved when the CMEA is incorporated [15,49]. Among all mixtures, BF-4E exhibits the most favorable performance, maintaining a CS of 27.36 MPa after 50 DWs, corresponding to a retention ratio of 54.17%. This synergistic improvement stems from the bimodal hydration behavior of the CaO-MgO system [21,22]. In the early stages, the formation of hydration products provides an immediate internal sealing effect, significantly reducing the initial porosity. During later ages, the fiber-matrix skeleton acts as a structural confinement cage, intercepting the delayed expansion of the CMEA. This interaction re-channels the expansion energy into a persistent compressive state across the ITZ [15,50]. This self-induced prestressing effect counteracts crystallization pressure and suppresses unstable crack propagation [25]. However, excessive CMEA incorporation leads to detrimental effects. For example, the CO-8E group shows a retention ratio of only 25.08% at 50 DWs, even lower than that of the control group. This indicates that over-expansion induces secondary cracking, accelerates the formation of connected transport pathways, and aggravates internal damage.

In the later stage of exposure (40–50 DWs), the rate of CS degradation gradually stabilizes for all FERC. At this stage, the surface matrix has undergone severe deterioration, and interconnected microcracks provide preferential pathways for sulfate ingress, driving the reaction front toward deeper regions toward the inner matrix [14]. Meanwhile, the substantial accumulation of corrosion products in localized regions results in a secondary filling effect [3,14,42], which partially delays further crack propagation. Although the delayed expansion potential of CMEA has been largely exhausted after extensive hydration, in optimized composite systems, the remaining intact fiber skeleton still provides effective residual bridging and pinning effects.

3.1.2. STS

Fig. 9 presents the evolution of STS and the corresponding retention ratio for all FERC during sulfate DWs. Similar to the CS behavior, a distinct three-stage pattern is observed. During the initial exposure period (0–10 DWs), all specimens exhibit a moderate increase in STS, ranging from 7% to 18%. Specifically, the CO and BF groups show strength increases of 16.01% and 10.14%, respectively. This enhancement is mainly related to the partial densification of the matrix caused by early-stage sulfate reactions [51]. The formation of limited amounts of corrosion products, together with continued hydration, contributes to the closure of pre-existing micro-defects, thereby improving tensile resistance. During the intermediate stage (10–40 DWs), the internal stresses induced by crystallization expansion gradually exceed the TS of the cementitious matrix, leading to a pronounced deterioration in tensile performance [46]. Owing to the high sensitivity of STS to internal damage evolution, the fiber-free CO group shows a pronounced reduction, with the retention ratio decreasing to 51.96% at 40 DWs. In contrast, fiber-reinforced systems exhibit a slower degradation rate. Among the mono-fiber systems, the BF group consistently exhibits superior tensile capacity compared to the PF group, as BF BFs effectively carry tensile stress at crack tips and restrain the propagation of macrocracks.

In fiber-CMEA composite systems, the combination of 4% CMEA and HF demonstrates outstanding synergistic crack resistance under tensile loading. The PB-4E group achieves a strength retention ratio of 84.16% at 30 DWs and maintains a high level of 72.60% even at 40 DWs. This behavior can be explained by the restrained expansion of CMEA under fiber confinement. The moderate CE is converted into compressive stress acting at the fiber-matrix interface [52], which enhances interfacial bonding and delays crack opening. Consequently, HF remain effective in carrying tensile loads even at relatively small crack widths. In contrast, increasing the CMEA dosage to 8% results in excessive expansion, generating uncontrolled internal stresses and inducing additional microcracking. As a result, the PB-8E system exhibits accelerated deterioration at later stages, indicating that over-expansion compromises tensile

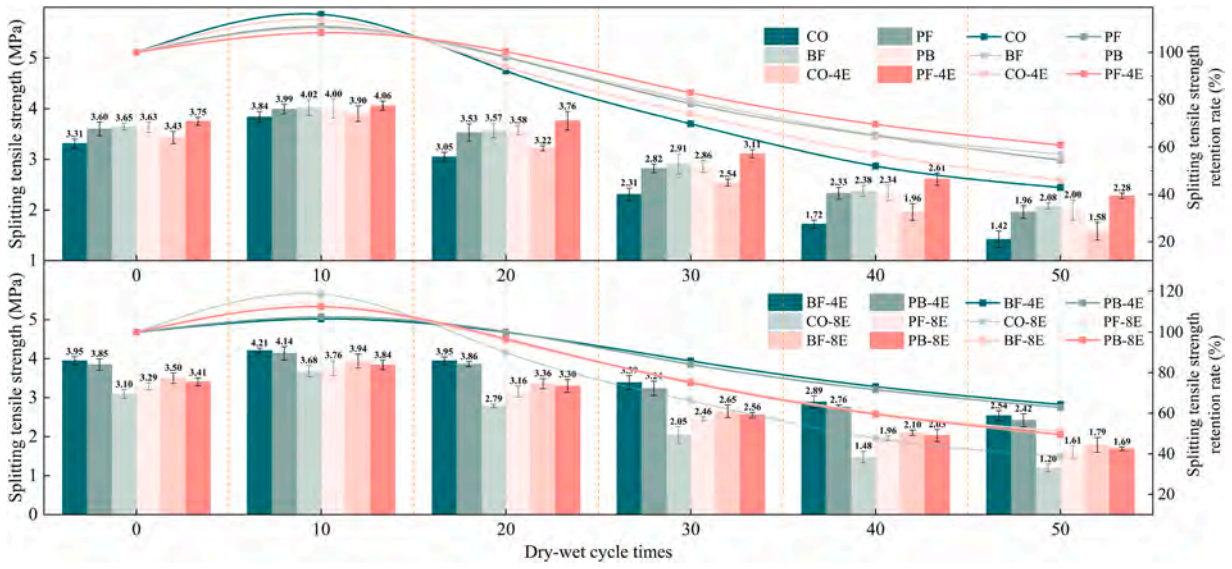

Fig. 9. STS and corresponding retention ratios of FERC with different mix proportions under sulfate DWs.

resistance.

During the final stage (40–50 DWs), the degradation rate gradually levels off for all mixtures. After 50 DWs, the STS of the PB-4E group remains 31.75% higher than that of the CO group, demonstrating that the combined action of HF and an appropriate CMEA dosage effectively preserves residual tensile capacity under prolonged SA.

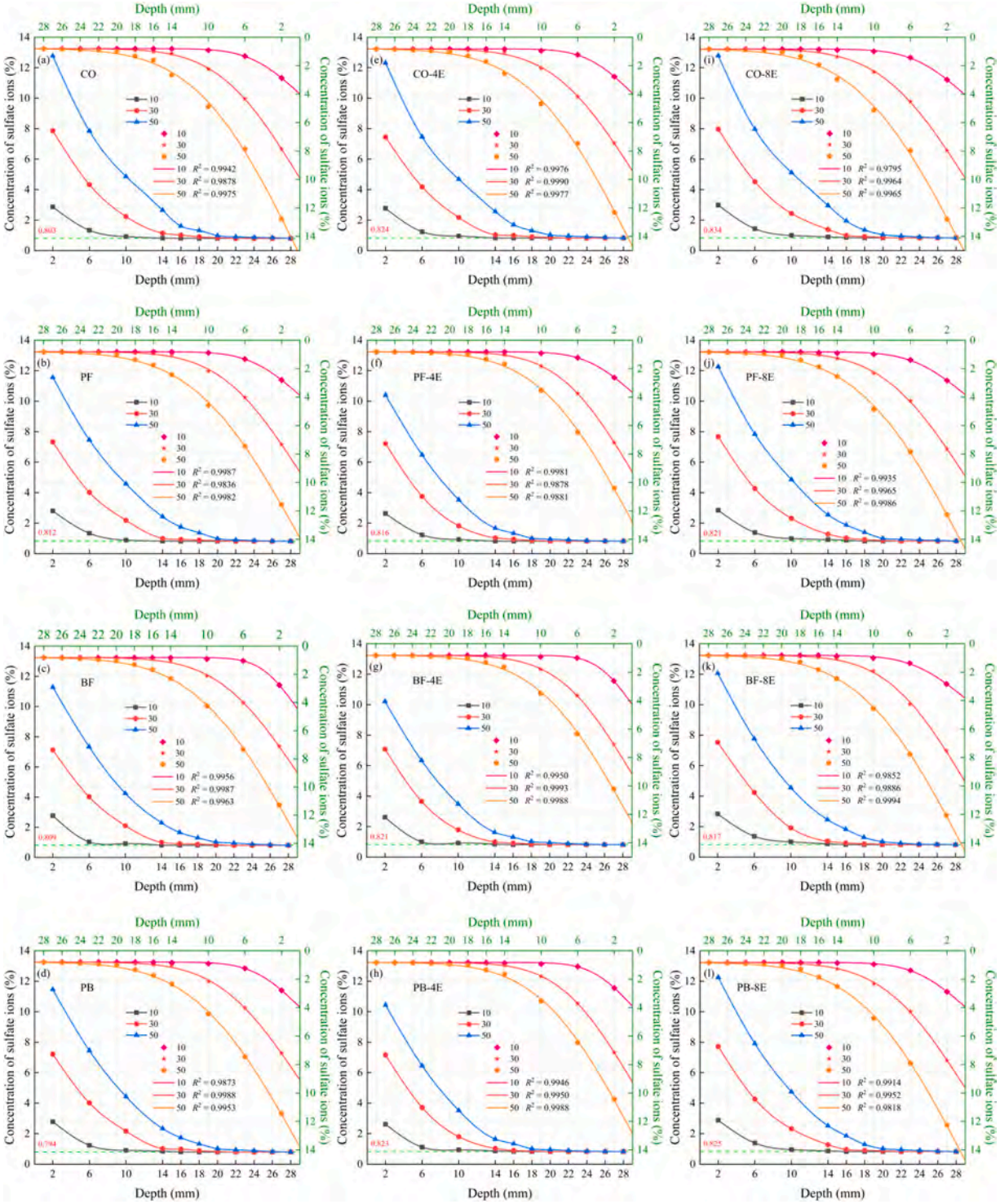

Fig. 10. Evolution of SO_4^{2-} concentration profiles in different specimens under sulfate DWs.

3.2. Analysis of SO_4^{2-} PD and diffusion behavior

3.2.1. SO_4^{2-} PD and distribution characteristics

Fig. 10 shows the SO_4^{2-} concentration profiles of all specimens after 10, 30, and 50 DWs. The distributions exhibit a typical non-steady-state diffusion characteristic [14], with concentration decreasing progressively from the exposed surface toward the interior. As exposure proceeds, the overall sulfate content within the matrix increases continuously, indicating sustained inward transport of aggressive ions. This behavior confirms that external aggressive ions primarily penetrate through surface capillary pores and accumulate significantly in the near-surface region. Taking the CO mixture as an example, the sulfate front advanced progressively with increasing cycle number. After 10 DWCs, the penetration depth was less than 16 mm, and the surface SO_4^{2-} mass fraction was 2.87%. After 50 DWCs, the penetration depth exceeded 26 mm, while the surface SO_4^{2-} mass fraction increased to 12.77%. This trend reflects the repeated evaporation of pore water during drying and the capillary absorption of sulfate solution during rewetting, which jointly promoted the inward transport of SO_4^{2-}. In contrast, the fiber-reinforced mixtures exhibited lower sulfate ingress. After 50 DWCs, the surface SO_4^{2-} mass fractions of both the single-fiber and PB mixtures were approximately 10% lower than that of the CO mixture, and their penetration depths were also smaller. This behavior was attributed to fiber-induced crack restraint, which reduced microcrack opening and connectivity, increased transport-path tortuosity, and consequently delayed the advance of the sulfate front [14].

On the basis of the fiber network, the introduction of an appropriate amount of CMEA further enhances chemical blocking. For instance, after 50 sulfate DWs, the surface concentration of the PF-4E group is approximately 10% lower than that of the PF group without CMEA. This is due to the moderate CE of 4% CMEA, which, under fiber confinement, effectively compacts the PS. However, when the dosage increases to 8%, the permeability resistance deteriorates. The PF-8E group exhibits a 6.01% higher surface concentration than the PF group, indicating that excessive CE exceeds the confinement capacity of fibers and induces secondary microcrack propagation [25–27]. These newly formed crack networks provide additional transport pathways for aggressive ions, ultimately weakening the sulfate resistance of the material.

3.2.2. Quantitative prediction and model fitting of sulfate diffusion depth

To further quantify SO_4^{2-} transport, concentration profiles were fitted using a nonlinear approach derived from Fick's second law. As indicated by the fitted curves in Fig. 10, good agreement is obtained across different exposure stages, confirming the applicability of the model. The R^2 for all fittings exceeds 0.97, demonstrating that the model can effectively capture the diffusion behavior under cyclic exposure conditions. The characteristics of the fitted curves provide direct insight into the ion-blocking capacity of different FERC. Relative to the CO group, both the HF (PB) and mixtures incorporating 4% CMEA exhibit steeper concentration gradients, reflecting a stronger resistance to ion penetration and a reduced effective diffusion depth. The calculated theoretical PD further confirm that, after 50 DWs, the erosion front of the PB-4E group is markedly shallower than that of the reference group.

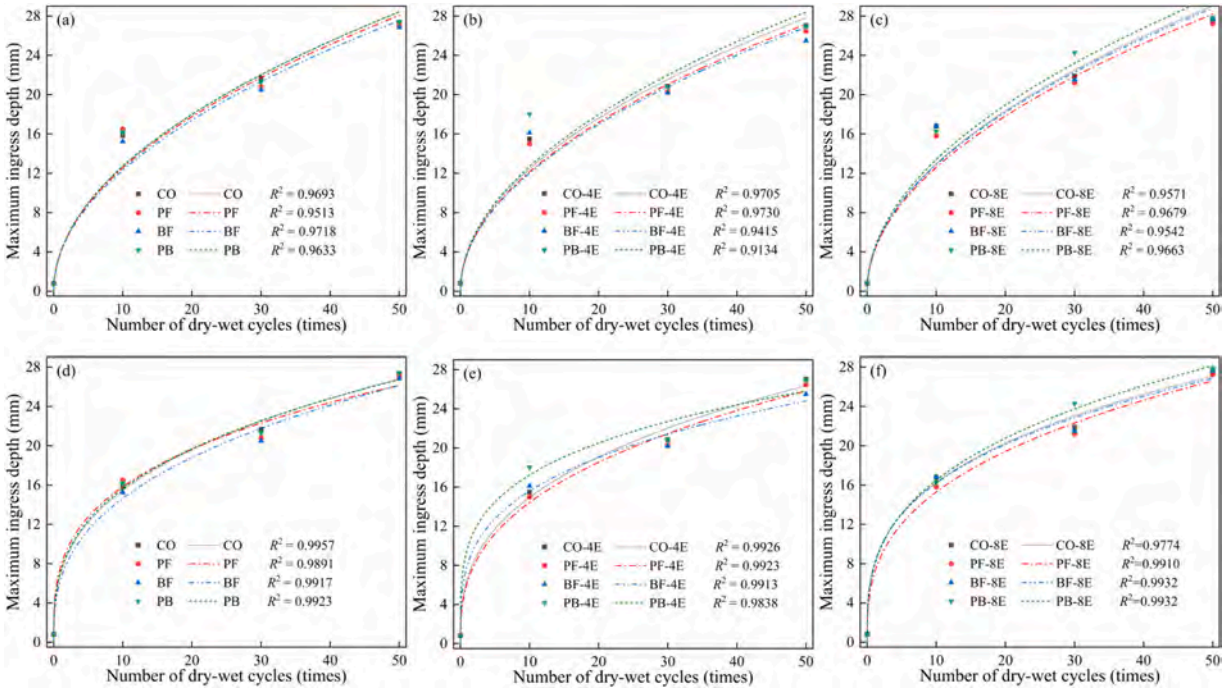

Fig. 11. Relationship between SO_4^{2-} PD and exposure time under different conditions.

3.2.3. Erosion kinetics models and applicability evaluation

The evolution of SO_4^{2-} penetration depth was analyzed using two approaches: the conventional square-root model and a time-dependent power-law model. The corresponding fitting results are presented in Fig. 11. The square-root model results are shown in Fig. 11(a)-(c), whereas Fig. 11(d)-(f) correspond to the power-law model. A comparative analysis indicates that the power-law formulation provides improved fitting performance, suggesting that sulfate transport under drying-wetting conditions exhibits pronounced time-dependent behavior. The R^2 for this model are all greater than 0.97, with some exceeding 0.99. In contrast, the square-root law model exhibits relatively lower fitting performance, with certain R^2 values falling below 0.95. The fitted theoretical parameters reveal substantial differences in permeability among the FERC. The PB group exhibits a significantly lower permeability coefficient compared to both mono-fiber systems and the reference group. Similarly, the composite systems incorporating 4% CMEA demonstrate the lowest permeability coefficients. These findings objectively confirm that the synergistic combination of HF and an appropriate dosage of CMEA effectively retards the inward progression of the erosion front.

3.3. ML under SA

Fig. 12 presents the evolution of ML ratios for all FERC subjected to sulfate DWs. The mass evolution of all specimens follows a three-stage trend, involving an initial increase, a subsequent rapid decline, and a final stabilization phase. During the early exposure period (0–10 DWs), all mixtures exhibit a slight mass gain. This behavior is associated with continued hydration of residual cement and FA, together with the partial filling of pore space by newly formed AFt and gypsum resulting from SO_4^{2-} ingress [46]. In particular, FERC incorporating CMEA exhibit more pronounced early-stage mass gain, as the accumulation of hydration products further accelerates the densification of surface micropores. During the intermediate stage (10–40 DWs), the specimens enter a phase of rapid ML. As exposure progresses, the accumulation of corrosion products within the PS leads to increasing crystallization-induced stress under repeated DWs. This physical wedging effect, coupled with the CE associated with AFt formation, leads to severe internal stress buildup. Once the combined stress exceeds the TS of the matrix, extensive surface spalling occurs. After 50 DWs, the ML ratio of the CO group reaches

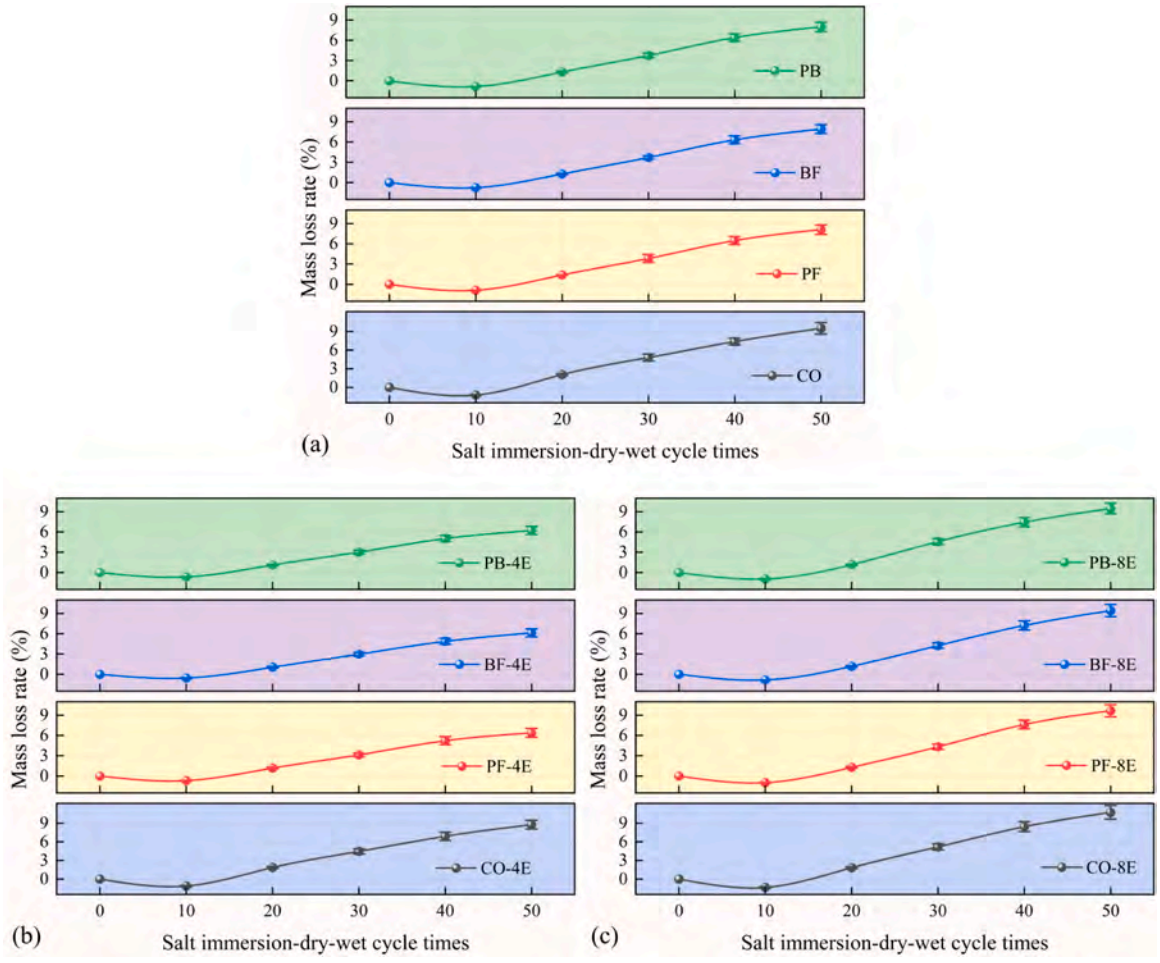

Fig. 12. Relationship between ML ratio and number of DWs for different FERC mixtures.

9.52%. In comparison, the system incorporating HF and 4% CMEA (PB-4E) shows enhanced resistance to material loss, with a ML ratio of only 6.21%, corresponding to a reduction of 34.77% relative to the CO group. This behavior can be explained by the combined effects of pore refinement and internal stress regulation. Specifically, the formation of $Ca(OH)_2$ and $Mg(OH)_2$ contributes to pore blocking, while the restrained CE under fiber confinement is converted into internal compressive stress, mitigating damage accumulation [15,53,54]. This synergistic effect significantly inhibits matrix fragmentation and spalling. By contrast, increasing the CMEA content to 8% leads to a deterioration in performance. The PB-8E mixture exhibits a ML ratio of 9.47%, comparable to that of the CO group, indicating that excessive expansion induces additional cracking and offsets the beneficial effects. This deterioration is caused by excessive expansion, which induces severe stress concentration, promotes extensive secondary cracking, and accelerates material spalling. In the later stage (40–50 DWs), the rate of ML gradually decreases for all FERC. This is mainly because the severely deteriorated surface layer has already spalled off, exposing a relatively denser inner matrix. Meanwhile, some corrosion products redeposit within deeper cracks, forming localized secondary densification zones that temporarily retard further surface degradation.

3.4. Electrical response of FERC under sulfate DWs

3.4.1. Macroscopic ER response to erosion

Fig. 13 presents the evolution of macroscopic ER of all specimens during 50 DWs. A clear stage-dependent evolution is observed for all FERC, characterized by an initial rise followed by a subsequent decline, with the 10th cycle marking the transition. During the initial exposure period (0–10 DWs), ER increases progressively for all mixtures. For example, the CO group shows an increase from 180.16 Ω·m to 227.00 Ω·m, corresponding to a 26.0% enhancement. The BF-8E mixture exhibits the highest peak value, reaching 282.92 Ω·m at the 10th cycle, which is 16.0% higher than its initial level. The early increase in ER reflected the coupled effects of pore refinement, reduced pore connectivity, increased transport-path tortuosity, and changes in pore-solution chemistry [55]. The formation and deposition of AFt, gypsum, and other hydration products may have partially occupied the pore space, while changes in the concentration and mobility of ions in the pore solution also affected electrical conduction [56]. Although BF-8E reached the highest absolute ER at 10 cycles, its relative increase of 16.0% was lower than the 26.0% increase observed for CO. Therefore, the higher absolute ER of BF-8E should not be interpreted as a more pronounced relative increase. Overall, the net increase in ER indicates that densification-related effects outweighed crack-induced conduction during the early stage, although their individual contributions cannot be distinguished from ER measurements alone. After approximately 10 DWs, the ER begins to decrease continuously, with high-dosage FERC showing more evident signs of damage. For instance, the ER of the CO group decreases from 227.00 Ω·m to 111.70 Ω·m, representing a reduction of 50.8%. Similarly, the BF-8E group, which initially exhibited the highest ER, shows a sharp decline in the later stage, dropping from 282.92 Ω·m to 168.29 Ω·m. This behavior is attributed to the transition from microstructural densification to macrocrack development. Repeated DWs induce significant crystallization pressure, and when this physical stress combines with accumulated CE and exceeds the TS of the matrix, the initially dense product layer rapidly deteriorates due to crack propagation. The resulting crack network provides low-resistance pathways for ion transport, whose effect outweighs the local pore-blocking action, thereby accelerating the reduction in macroscopic ER.

A comparison of CMEA dosage levels reveals that mixtures with optimized incorporation (e.g., BF-4E and PB-4E) demonstrate enhanced long-term stability. As illustrated in Fig. 13, the BF-4E mixture retains an ER of 175.39 Ω·m after 50 DWs, representing the highest value among all FERC, while also exhibiting the slowest rate of degradation during the later stage. The relatively high retained ER of BF-4E may be associated with the restraint of CMEA-induced deformation by the three-dimensional fiber network. By limiting crack opening and interfacial separation, the fiber network is likely to help preserve contact within the matrix and ITZ and delay the

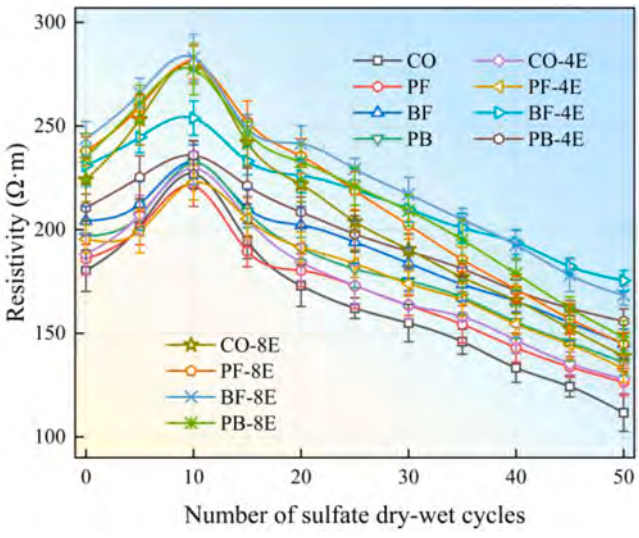

Fig. 13. Evolution of ER of FERC under sulfate DWs.

transition to a damage-dominated state [25,27]. In contrast, excessive incorporation of CMEA (8%) results in uncontrolled CE, which exceeds the confinement capacity of the fiber network. This leads to severe secondary cracking within the matrix and ultimately accelerates the degradation of durability performance.

3.4.2. Damage characterization based on impedance characteristics

(1) **Impedance spectral characteristics and equivalent circuit model**

EIS can characterize changes in the internal structure of cement-based materials through pore-solution conduction, interfacial polarization, and ion diffusion. Fig. 15 presents the Nyquist plots of the CO, BF, and BF-4E specimens after 0, 10, 30, and 50 sulfate DWs. The impedance spectra of all groups consist of a depressed capacitive arc in the high-frequency region and an inclined diffusion tail in the low-frequency region. Their shapes and characteristic dimensions change markedly with increasing cycle number, indicating continuous evolution of the conductive pathways, pore-solution properties, and solid-liquid interfacial state within the specimens.

To interpret these impedance responses, the conductive pathways within the specimens were classified into continuous conductive paths, discontinuous conductive paths, and insulator conductive paths according to the microstructural conduction model shown in Fig. 14(a) [43]. Continuous conductive paths (CCPs) consist primarily of interconnected capillary pores and provide the main channels for ion transport through the pore solution. Discontinuous conductive paths (DCPs) comprise pores interrupted by the cementitious matrix or local discontinuities, and charge transport along these paths must overcome greater local resistance. Insulator conductive paths (ICPs) mainly correspond to dense hydration products and regions with low pore connectivity and therefore exhibit high electrical resistance.

Based on the impedance spectral characteristics and the conductive-path model, the EIS data were fitted using the equivalent circuit shown in Fig. 14(b). The total impedance is expressed as [57]:

$$Z = R_1 + \frac{1}{j\omega C + \frac{1}{R_2 + Z_Q} + \frac{1}{R_{ct} + Z_W}} \tag{12}$$

where R_1 is the series bulk resistance, which is jointly affected by the pore-solution resistivity and the connectivity of continuous conductive paths; C represents the dielectric polarization response of the system; R_2 and the constant phase element (Q) jointly describe the nonideal capacitive behavior associated with discontinuous conductive paths and pore-structure heterogeneity; R_{ct} is the charge-transfer resistance, which reflects resistance to charge exchange at the solid-liquid interface; and Z_W is the Warburg impedance used to characterize ion diffusion in the low-frequency region.

Because of the heterogeneity of the pore and interfacial structures, the Q was used to describe the dispersion of the impedance response. Its impedance is given by:

$$Z_Q = \frac{1}{Y_0 (j\omega)^n} = \frac{1}{Y_0}\left(\cos\frac{n\pi}{2} - j\sin\frac{n\pi}{2}\right) \tag{13}$$

where Y_0 is the admittance parameter and n is the dispersion exponent. More specifically, R_2 represents the resistance of the residual solution within the pores. The interfacial Faradaic process is represented by the series connection of the charge-transfer resistance R_{ct} and the Warburg element W. The Warburg impedance describes ion diffusion and is calculated as:

$$Z_W = \frac{\sigma}{\sqrt{\omega}}(1 - j) \tag{14}$$

where σ is the Warburg coefficient. Finally, nonlinear fitting of the EIS spectra at all measurement stages was performed using ZView 3.1. The principal electrochemical parameters obtained from the fitting are listed in Table 8.

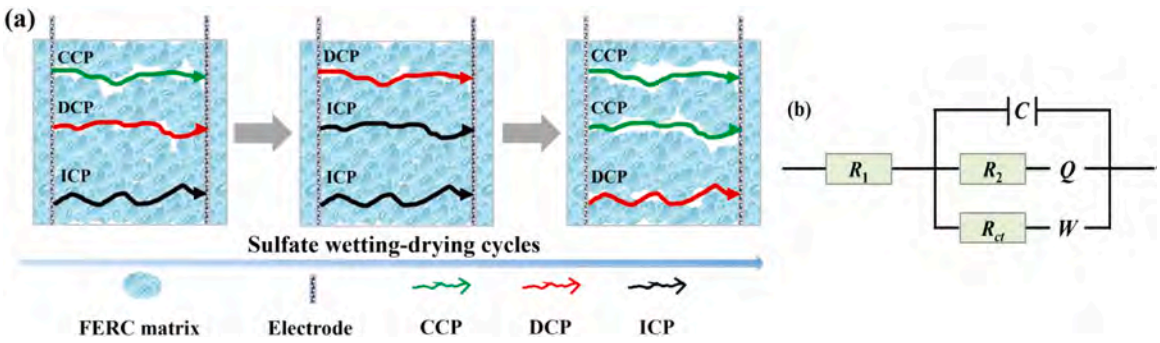

Fig. 14. Conductive pathways and equivalent circuit model of FERC microstructure.

(2) **Response of impedance parameters to damage induced by sulfate DWs**

EIS uses alternating electrical signals to sensitively track changes in liquid-phase connectivity and solid-liquid interfaces within the matrix. Under sulfate DWs, the evolution of the matrix impedance is associated with changes among the three microscopic conductive pathways. Fig. 15 presents the Nyquist plots of the CO, BF, and BF-4E specimens after 0, 10, 30, and 50 DWs. All measured spectra consist of a capacitive arc in the high-frequency region and a diffusion tail in the low-frequency region [43,44,57].

During the first 10 cycles, R_1 of the CO, BF, and BF-4E specimens increased from 8733, 9743, and 11,878Ω to 10,473, 12,908, and 11,946Ω, respectively, corresponding to increases of 19.93%, 32.49%, and 0.57%. These results indicate an increase in the overall resistance to electrical conduction during the initial stage of sulfate exposure. The cycle stage, moisture condition, and testing temperature of the specimens were controlled consistently before each measurement, thereby reducing interference from differences in testing conditions. Nevertheless, R_1 remained dependent on both PS and pore-solution chemistry [58]. At the initial stage, continued hydration and the limited precipitation of solid products, including AFt and gypsum, occupied part of the capillary pores and interfacial defects. This reduced the effective cross-sectional area available for conduction, increased transport tortuosity, and decreased pore connectivity. Consequently, the formation factor of the pore network increased, corresponding in the equivalent conductive-path model to a lower proportion of CCPs and a higher proportion of DCPs. Meanwhile, the incorporation of ingressing SO_4^{2-} into sulfate-bearing crystalline phases transferred part of the sulfate from the liquid phase to the solid phase, altering the concentration and composition of effective charge carriers in the pore solution. By contrast, the continued ingress of external Na + and SO_4^{2-} could increase the ionic strength of the pore solution and enhance electrical conduction. The measured variation in R_1 therefore represents the combined evolution of pore-network geometry and pore-solution electrochemical properties. During the initial stage of exposure, the resistance increase caused by a smaller effective conduction area, reduced pore connectivity, greater transport tortuosity, and changes in liquid-phase conductivity associated with sulfate binding collectively outweighed the conductive enhancement caused by external electrolyte ingress. The evolution of R_{ct} differed among the material systems over the same period. R_{ct} decreased by 18.15% and 19.01% in CO and BF-4E, respectively, but increased by 118.23% in BF. These differences indicate that early sulfate-bearing product formation, interfacial polarization, and local liquid-phase transport were jointly affected by material composition and the initial PS. The different trends of R_1 and R_{ct} further demonstrate that high-frequency bulk conduction and charge transfer across the solid-liquid interface represent distinct physical processes. Considering the concurrent increase in macroscopic ER and early improvement in mechanical performance, the increase in R_1 primarily reflects the higher pore-network formation factor resulting from limited solid-product filling, while changes in pore-solution ion composition provide a non-negligible liquid-phase contribution. Therefore, the early increase in R_1 is neither an exclusive electrical signature of CCP-to-DCP conversion nor solely attributable to the increase in pore-solution resistivity caused by sulfate binding. Instead, it reflects the coupled effects of pore-network reconstruction and changes in liquid-phase ion-transport characteristics.

As the number of cycles increased from 30 to 50, the Nyquist plots of all groups shifted toward the low-impedance region, with the most pronounced reduction observed in CO. After 50 cycles, R_1 of CO decreased from its initial value of 8733Ω to 5074Ω, corresponding to a reduction of 41.90%. Meanwhile, R_{ct} decreased from 31,797Ω to 7378Ω, retaining only 23.20% of its initial value. The concurrent decreases in R_1 and R_{ct} indicate enhanced bulk conductivity and a substantial reduction in charge-transfer resistance at the solid-liquid interface. As physical crystallization pressure and CE stress continued to accumulate, microcracks propagated from pore walls and interfacial regions into the matrix and gradually interconnected. This increased the effective cross-sectional area for electrical conduction, reduced transport tortuosity, and decreased the pore-network formation factor. The penetration of the exposure solution through newly formed cracks further increased the concentration of mobile ions in the local pore solution. Both effects contributed to the decrease in bulk resistance and appeared in the equivalent conductive network as an increased relative contribution of CCPs. In contrast, R_2 varied nonmonotonically during cycling. For example, R_2 of CO decreased from an initial value of 21,825Ω to 12,893Ω after 30 cycles and subsequently increased to 17,774 Ω after 50 cycles. Similar stage-dependent fluctuations were observed in BF and BF-4E. R_2 is associated with discontinuous conductive paths, local pore-solution redistribution, and heterogeneous polarization. Its evolution is governed not only by pore size and connectivity but also by changes in interfacial moisture condition and ion concentration. Therefore, R_2 cannot independently characterize the extent of damage and should be interpreted together with R_1, R_{ct},

Table 8
Fitted EIS resistance parameters of the FERC specimens under sulfate DWs.

	R_1	R_2	R_{ct}
CO-0	8733	21825	31,797
CO-10	10,473	16,366	26,027
CO-30	8116	12,893	12,283
CO-50	5074	17,774	7378
BF-0	9743	17,037	19,869
BF-10	12,908	37,755	43,361
BF-30	8404	17,404	13,399
BF-50	7727	11,145	10,117
BF-4E-0	11,878	32,971	41,373
BF-4E-10	11,946	18,937	33,510
BF-4E-30	11,609	17,515	33,489
BF-4E-50	9350	22,060	23,898

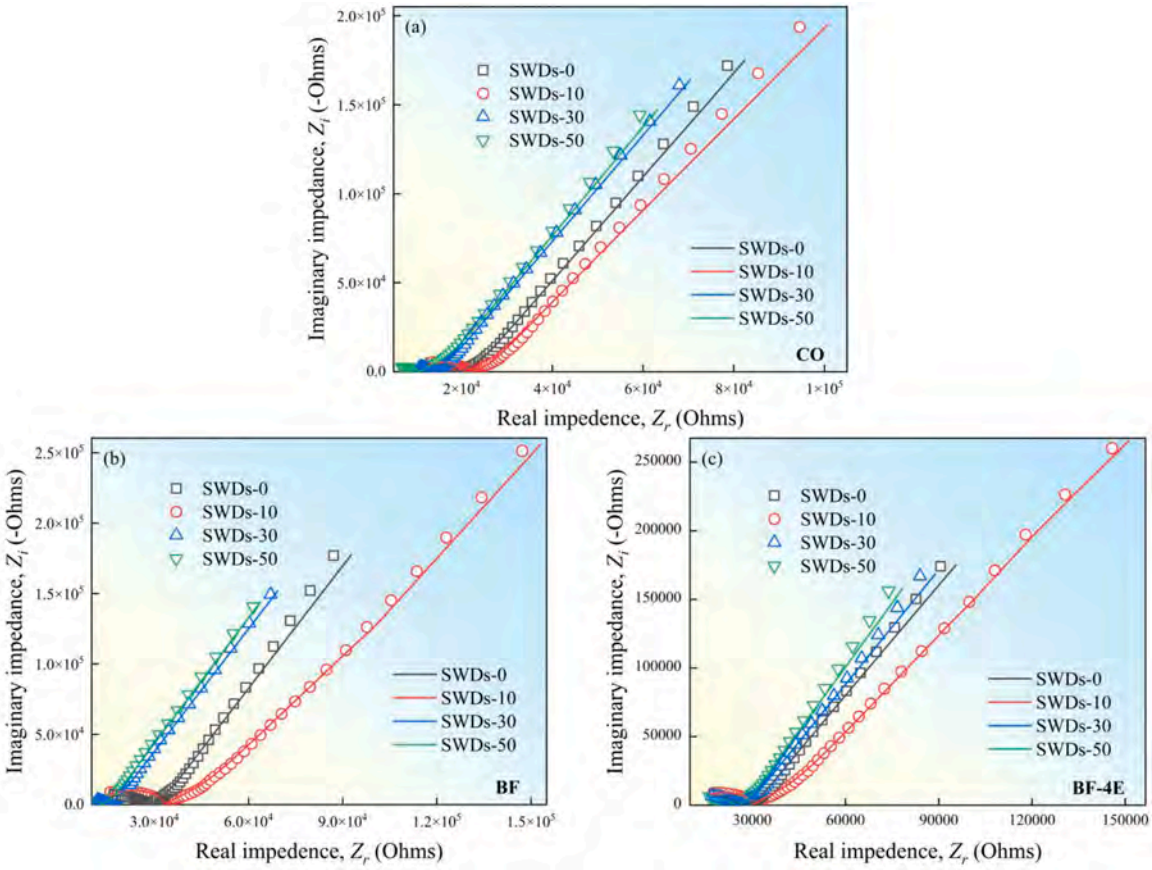

Fig. 15. Nyquist plots of FERC under sulfate DWs.

and macroscopic ER.

Compared with CO and BF, BF-4E maintained a higher impedance level during the intermediate and later stages of sulfate exposure. After 50 cycles, its R_1 and R_{ct} values were 9350 and 23,898Ω, respectively. Both values were higher than those of CO and BF at the same exposure stage. These results indicate that BF-4E retained greater resistance to bulk transport and charge exchange at the solid-liquid interface after prolonged cycling. This behavior can be attributed to the synergistic effects of CMEA hydration and crack control by BF. At an appropriate dosage, the $Ca(OH)_2$ and $Mg(OH)_2$ generated by CMEA hydration fill part of the capillary pores and interfacial defects, thereby reducing the effective connectivity of the pore network. BF restrains crack opening and interconnection through crack bridging, pinning, and interfacial bonding. The distributed restraint provided by the fiber network also converts part of the free CMEA-induced expansion into restrained expansion, improving contact within the matrix and interfacial regions. Together, these mechanisms maintain a relatively high pore-network formation factor and delay the re-establishment of low-resistance CCPs. Consequently, BF-4E retained higher R_1 and R_{ct} values after 50 cycles.

3.5. *Phase assemblage and chemical bonding characteristics of FERC after sulfate DWs*

Fig. 16 presents the fitted XRD patterns, normalized semi-quantitative compositions of the selected crystalline phases, and FTIR spectra of FERC specimens after 50 sulfate DWs. Phase identification and pattern fitting revealed AFt, $CaSO_4{\cdot}2\,H_2O$, $Ca(OH)_2$, $Mg(OH)_2$, and SiO_2 as the major crystalline phases in all specimens. AFt and gypsum are the principal sulfate-bearing phases associated with sulfate reactions. $Ca(OH)_2$ originates mainly from cement hydration and the continued hydration of CaO in CMEA, whereas $Mg(OH)_2$ is associated with the hydration of MgO in CMEA. Quartz is derived primarily from the aggregates and fly ash. To compare the relative distributions of crystalline phases among the different mixtures, normalized semi-quantitative analysis was performed for four selected phases: AFt, gypsum, $Ca(OH)_2$, and $Mg(OH)_2$. Within the BF series, the combined relative proportion of AFt and gypsum decreased from 50.1% in BF to 41.4% in BF-4E and then increased to 57.8% in BF-8E. Relative to BF, BF-4E exhibited higher normalized relative proportions of both $Ca(OH)_2$ and $Mg(OH)_2$. When the CMEA dosage increased from 4% to 8%, the relative proportion of $Ca(OH)_2$ decreased, whereas that of $Mg(OH)_2$ increased further. These results indicate that the BF series exhibited a non-monotonic dosage-dependent redistribution of the selected crystalline phases.

The PB series exhibited a similar trend, as shown in Fig. 16(b). In PB, the relative proportions of AFt and gypsum were 33.1% and

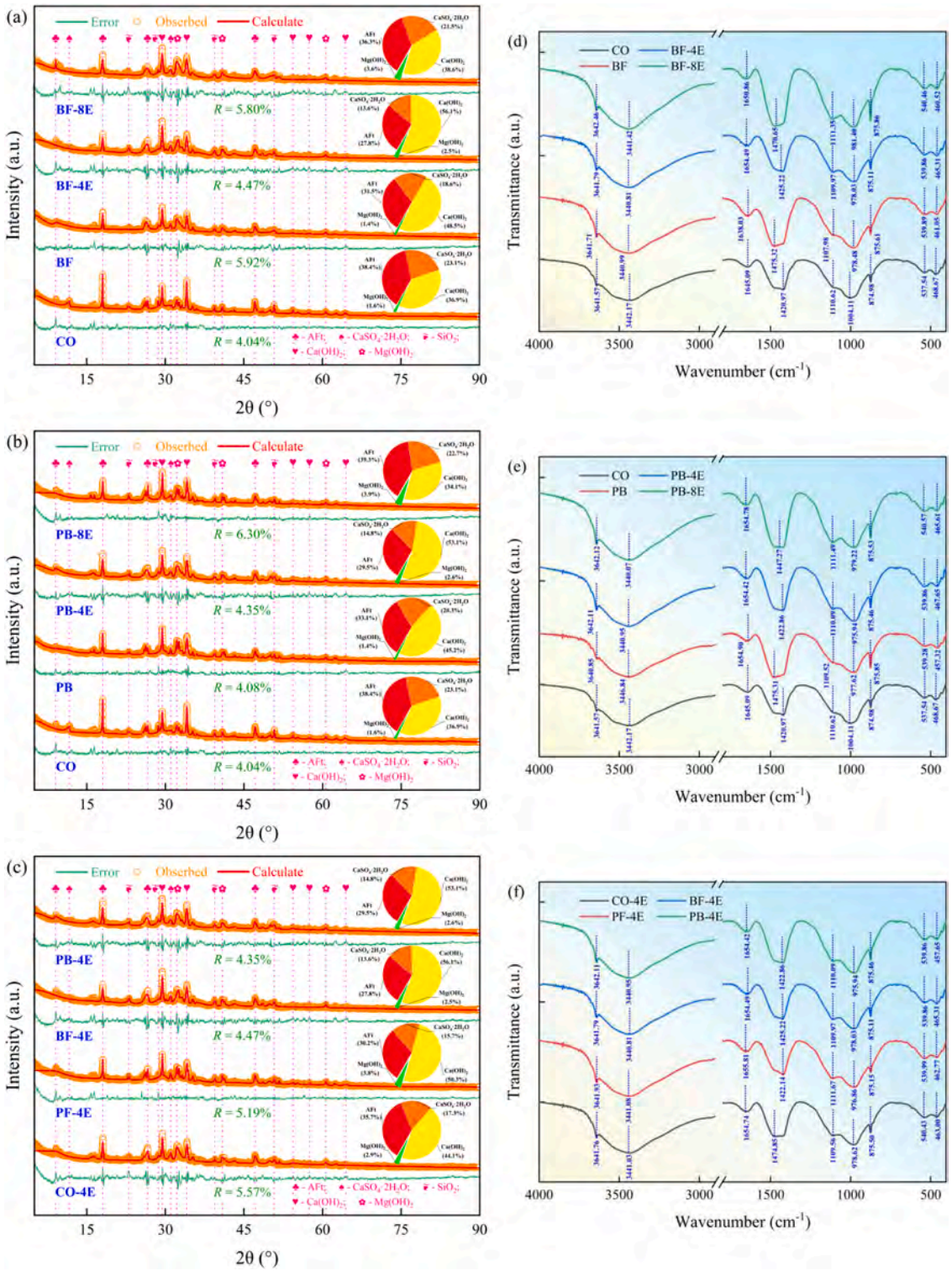

Fig. 16. Phase assemblage and chemical bonding characteristics of FERC specimens after 50 sulfate DWs: (a)-(c) fitted XRD patterns and normalized semi-quantitative results for the selected crystalline phases; (d)-(f) FTIR spectra. (a, d) BF-CMEA systems; (b, e) PB-CMEA systems; and (c, f) different fiber systems containing 4% CMEA.

20.3%, respectively, giving a combined proportion of 53.4%, which was 8.1 %age points lower than that of CO. Meanwhile, the relative proportion of $Ca(OH)_2$ increased from 36.9% in CO to 45.2% in PB. With the incorporation of 4% CMEA, the relative proportions of AFt and gypsum in PB-4E decreased to 29.5% and 14.8%, respectively. Their combined proportion decreased to 44.3%, 9.1 %age points lower than that in PB. Concurrently, the relative proportions of $Ca(OH)_2$ and $Mg(OH)_2$ increased from 45.2% to 53.1% and from 1.4% to 2.6%, respectively. When the CMEA dosage was increased to 8%, the relative proportions of AFt and gypsum in PB-8E reached 39.3% and 22.7%, respectively. Their combined proportion increased to 62.0%, 17.7 %age points higher than that in PB-4E. In contrast, the relative proportion of $Ca(OH)_2$ decreased from 53.1% to 34.1%, whereas that of $Mg(OH)_2$ increased from 2.6% to 3.9%. The consistent dosage-dependent trends observed in the BF and PB series indicate that 4% and 8% CMEA resulted in two distinctly different relative distributions of the selected crystalline phases. Fig. 16(c) further compares the effects of fiber type at a fixed CMEA dosage of 4%. The combined relative proportion of AFt and gypsum was 53.0% in CO-4E, compared with 45.9%, 41.4%, and 44.3% in PF-4E, BF-4E, and PB-4E, respectively. The corresponding relative proportions of $Ca(OH)_2$ were 44.1%, 50.3%, 56.1%, and 53.1%. No additional major crystalline phases were detected in the different fiber systems, although the relative distributions of the selected phases varied markedly. Among these mixtures, BF-4E exhibited the lowest combined proportion of AFt and gypsum and the highest proportion of $Ca(OH)_2$, followed by PB-4E.

The FTIR spectra shown in Fig. 16(d)-(f) further characterize the principal chemical bonding features of the specimens after sulfate DWs. All specimens exhibited a sharp absorption band at approximately 3641–3642 cm^{-1}, which is assigned to O-H stretching in $Ca(OH)_2$ and is consistent with the $Ca(OH)_2$ phase identified by XRD [59]. The broad band at approximately 3440–3447 cm^{-1} and the band at approximately 1638–1656 cm^{-1} are attributed to O-H stretching of bound or adsorbed water and H-O-H bending, respectively [59,60]. These bands are mainly associated with hydrated phases such as calcium silicate hydrate (C-S-H) gel, AFt, and gypsum. The bands at approximately 1421–1475 cm^{-1} and 875 cm^{-1} correspond to the asymmetric stretching and out-of-plane bending vibrations of CO_3^{2-} [61], respectively, indicating the presence of carbonate phases after cycling. All specimens exhibited a composite absorption envelope within approximately 900–1200 cm^{-1}, arising from overlapping vibrations of sulfate and silicate structures [59]. In the CMEA-containing specimens, the feature at approximately 1110 cm^{-1} is assigned to the asymmetric stretching vibration of S-O bonds in SO_4^{2-} and is associated with sulfate-bearing phases such as AFt and gypsum [59]. The band at approximately 976–1004 cm^{-1} is mainly attributed to the asymmetric stretching vibration of Si-O bonds in C-S-H gel [62]. The band at approximately 538–541 cm^{-1} is associated with Al-O vibrations in octahedrally coordinated aluminate environments, whereas that at approximately 457–469 cm^{-1} is primarily assigned to the bending vibrations of Si-O-Si or O-Si-O bonds in silicate structures [60,62]. The concurrent presence of absorption bands associated with SO_4^{2-}, Al-O, and bound water is consistent with the hydrated sulfoaluminate phases, including AFt, identified by XRD.

As shown in Fig. 16(d) and (e), the principal FTIR absorption bands of the BF and PB series remained unchanged with varying CMEA dosage, indicating that the mixtures contained the same major types of hydration products and sulfate-bearing phases. After CMEA incorporation, the SO_4^{2-} vibration at approximately 1110 cm^{-1} and the Si-O vibration at approximately 976–981 cm^{-1} became more clearly resolved within the composite absorption envelope. However, no additional major characteristic bands appeared when the CMEA dosage increased from 4% to 8%. These results indicate that the CMEA dosage primarily altered the relative distribution of the existing phases without changing the main types of products formed after sulfate exposure. At a fixed CMEA dosage of 4%, CO-4E, PF-4E, BF-4E, and PB-4E exhibited the same principal FTIR absorption bands, as shown in Fig. 16(f). This finding indicates that fiber type did not alter the characteristic chemical bonding environments of the main hydration products and sulfate reaction products. Combined with the XRD results in Fig. 16(c), the differences among the fiber systems were mainly reflected in the relative distributions of the selected crystalline phases rather than in the formation of additional major crystalline phases or new types of chemical bonds.

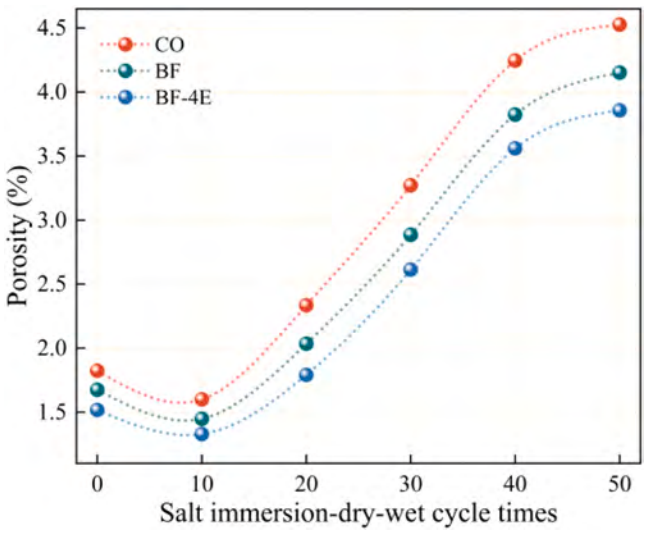

Fig. 17. Variation of total porosity with sulfate DWs for different specimens.

In summary, the normalized semi-quantitative XRD results demonstrate that CMEA dosage markedly affected the relative distributions of the selected crystalline phases in FERC after sulfate DWs. The mixtures containing 4% CMEA exhibited lower combined proportions of AFt and gypsum and higher proportions of $Ca(OH)_2$. When the CMEA dosage was increased to 8%, the relative proportions of AFt, gypsum, and $Mg(OH)_2$ increased, whereas that of $Ca(OH)_2$ decreased, consistent with the deterioration in later-age performance. The FTIR results further confirmed the presence of

$Ca(OH)_2$, C-S-H, sulfate groups, and carbonate phases. Neither CMEA dosage nor fiber type altered the main types of reaction products. Based on the chemical composition of CMEA and the actual mixture proportions, the net increases in SO_3 equivalent introduced by 4% and 8% CMEA relative to CO were 2.03 and 4.06 kg/m^3, respectively. The increase in the 8% CMEA mixtures was twice that in the 4% CMEA mixtures. Under sulfate DWs, sulfate-bearing components in CMEA may be progressively released. Together with the development of a microcrack network induced by excessive expansion, this process promotes coupled deterioration associated with internal sulfate supply and external sulfate ingress, thereby increasing AFt and gypsum formation and accelerating $Ca(OH)_2$ consumption. The deterioration of the mixtures containing 8% CMEA can therefore be attributed to the combined effects of a larger internal sulfate reserve, CE stresses, and the loss of effective restraint provided by the fiber network.

3.6. Evolution of the PS and microstructure of FERC under sulfate DWs

3.6.1. Dynamic evolution of porosity and PS

Fig. 17 illustrates the evolution of total porosity of all specimens as a function of sulfate DWs. The evolution of porosity with increasing DWs exhibits a two-stage response, involving an initial reduction followed by a progressive increase. During the early exposure period (0–10 DWs), all mixtures show a slight decrease in total porosity. Specifically, the porosity of the CO group decreases from an initial value of 1.82–1.60%. This behavior is associated with continued hydration and the partial occupation of pore space by early-formed AFt and gypsum, leading to a temporary densification of the matrix [14]. However, with the progression of sulfate DWs (10–50 DWs), the continuous accumulation of reaction products deposited within the pores, coupled with sulfate supersaturation and crystallization induced by cyclic wetting and drying, leads to significant deterioration. As deterioration advances, the combined action of crystallization-induced stress and CE progressively exceeds the tensile resistance of the matrix, triggering widespread microcracking. The development and interconnection of these cracks significantly enhance transport connectivity, thereby accelerating

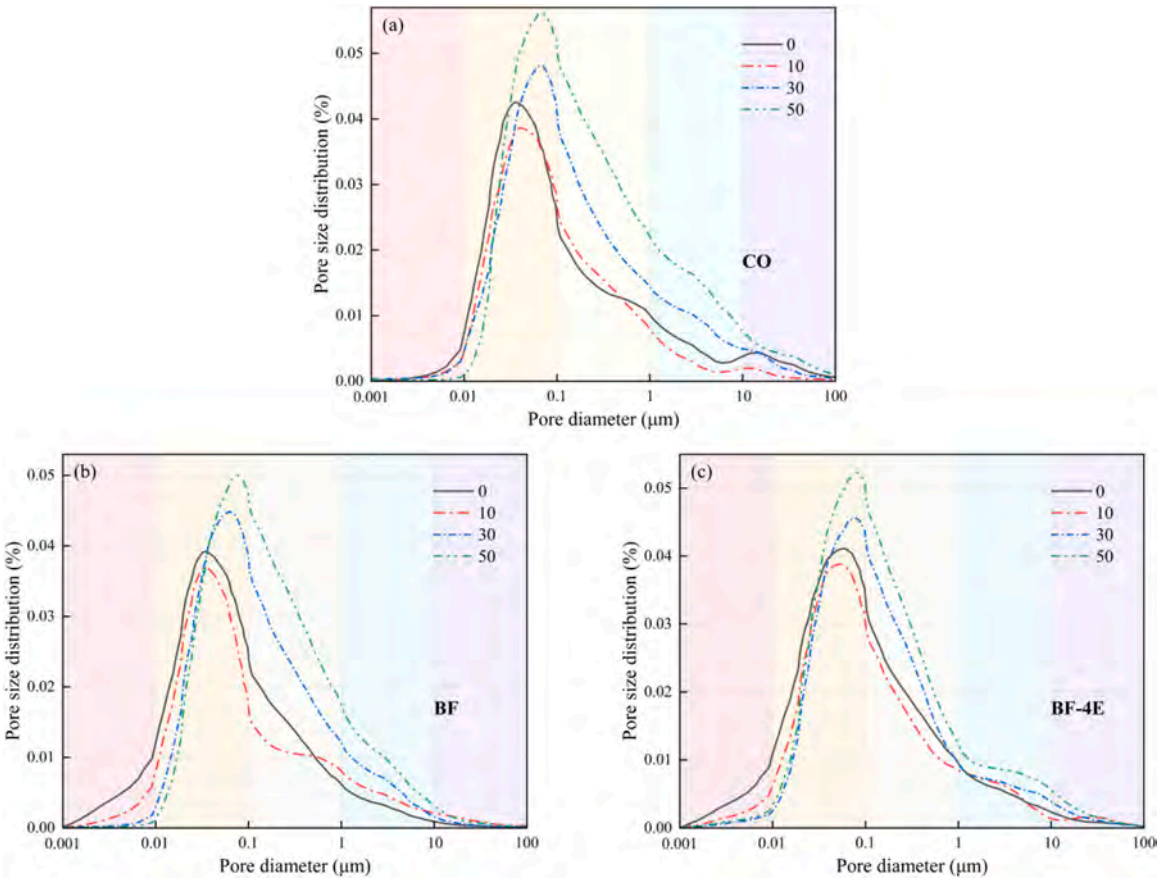

Fig. 18. Dynamic evolution of PS of FERC under sulfate DWs.

sulfate ingress and reversing the densification trend. After 50 DWs, the total porosity values of the BF and BF-4E groups are effectively controlled at 4.15% and 3.86%, corresponding to reductions of 8.39% and 14.79%, respectively, relative to the CO group. This improvement arises from the dual effects of pore refinement and transport inhibition induced by

CMEA hydration products, which limit ion penetration and reduce the available space for expansive reactions. This improvement can be attributed to the hydration products of the CMEA, which effectively seal micro-pores and reduce both the ingress rate of aggressive ions and the driving force for expansion. Meanwhile, the three-dimensional bridging network formed by high-modulus BF provides mechanical restraint, effectively inhibiting the propagation of microcracks induced by expansion stresses.

Figs. 18 and 19 illustrate the dynamic evolution of PS in FERC under SA. According to their influence on durability, pores are categorized into four ranges: harmless (<0.1 μm), less harmful (0.1–1 μm), harmful (1–10 μm), and seriously harmful (10–100 μm) [15]. With increasing exposure DWs, the PS exhibits a clear coarsening trend, characterized by a transformation from fine to coarse pores. For the CO group, prolonged exposure results in a marked coarsening of the pore system. The fraction of harmless pores decreases from 51.16% to 41.16%, while seriously harmful pores increase from 4.92% to 7.83%. Meanwhile, the pore size distribution curve shifts toward larger diameters, accompanied by the emergence of a secondary peak beyond 10μm. This behavior reflects progressive pore wall degradation and the coalescence of smaller pores into larger defects under sustained internal stress. By contrast, the BF-4E system exhibits a significantly more stable PS. The shift toward larger pore sizes is effectively restrained, and the pore system remains relatively compact. After 50 DWs, harmless pores still account for 53.14%, while seriously harmful pores are limited to 4.21%. This improved stability may be attributed to the combined effects of pore filling by CMEA hydration products and fiber-mediated restraint of crack opening and coalescence, which together limited pore coarsening [28,63].

To quantitatively characterize the geometric heterogeneity of the pore network during deterioration, the thermodynamic fractal dimension was calculated [15,45], as shown in Fig. 20. After 50 sulfate DWCs, CO exhibited the highest D value of 2.74, whereas BF-4E exhibited the lowest value of 2.61, indicating a less geometrically complex pore network under the adopted fractal model. Linear regression revealed strong positive correlations of D with total porosity and average pore diameter, with R^2 values of 0.9937 and 0.9979, respectively. These relationships indicate that pore coarsening was accompanied by increasing geometric heterogeneity.

3.6.2. *Microstructural morphology analysis*

Fig. 21 presents the SEM microstructural features of all specimens after 50 sulfate DWs. As illustrated in Fig. 21(a), extensive accumulation of needle-like AFt, plate-like gypsum, and $Na_2SO_4{\cdot}10\ H_2O$ crystals is observed within the pore space, accompanied by severe disruption of the C-S-H gel network. This indicates that the coupled effects of crystallization pressure and CE progressively undermine matrix integrity in the absence of effective regulation [64,65]. In contrast, Fig. 21(b) reveals the presence of abundant plate-like $Ca(OH)_2$ crystals, confirming that the CMEA provides an effective alkalinity buffering reservoir. However, due to the lack of a fiber-reinforced bridging network, distinct microcracks are still observed within the matrix. This suggests that the CE induced by CMEA is not effectively transformed into beneficial compressive pre-stress. As shown in Fig. 21(d), the matrix-fiber interface exhibits a porous and loose morphology accompanied by penetrating cracks. These cracks and their surrounding regions are densely filled with $Na_2SO_4{\cdot}10\ H_2O$ and AFt. The BF system exhibits a loose interfacial morphology with penetrating cracks, indicating insufficient resistance to expansion-induced damage. Similarly, debonding gaps are evident at the PF-matrix interface due to relatively weak interfacial bonding. These interfacial defects rapidly evolve into preferential pathways for SO_4^{2-} transport and are progressively widened by the precipitation of $Na_2SO_4{\cdot}10\ H_2O$ crystals, ultimately leading to the failure of fiber bridging.

In contrast, the incorporation of 4% CMEA markedly improves interfacial characteristics. As shown in Fig. 21(h), the surface of PF

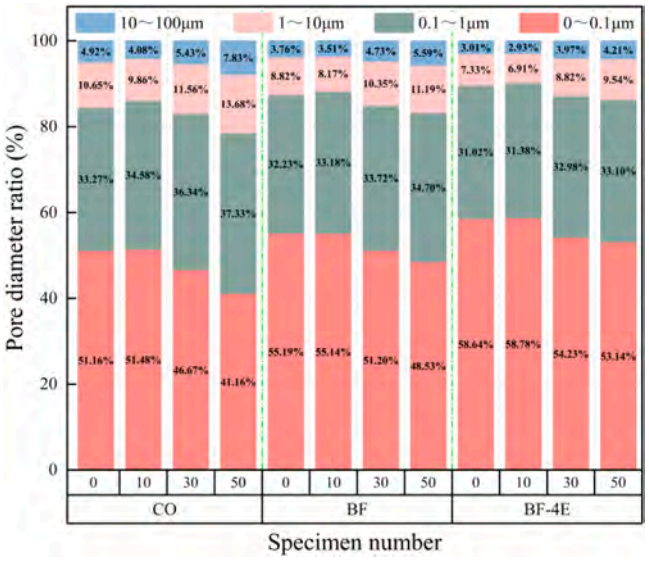

Fig. 19. Pore size distribution of different specimens under sulfate DWs.

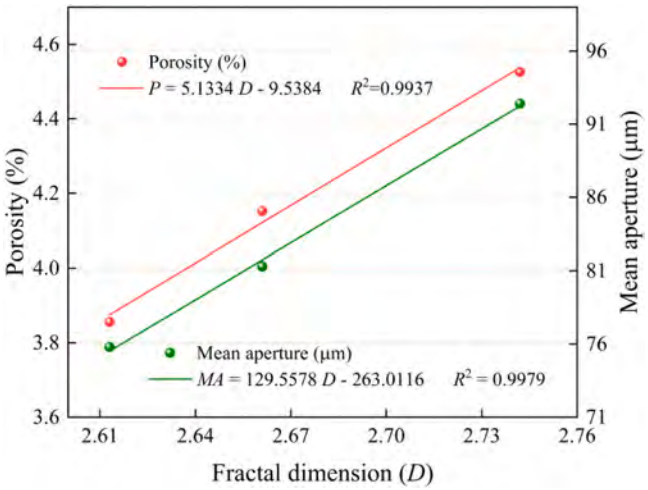

Fig. 20. PS-related parameters of different groups.

is densely coated with fine AFt, $Ca(OH)_2$, and flocculent $Mg(OH)_2$, resulting in a markedly densified ITZ. This enhancement is attributed to two synergistic effects: fibers act as preferential nucleation sites for CMEA hydration products and early-stage corrosion products [25,27,50], and the moderate CE generated by CMEA is transformed into restrained expansion under the confinement of the HF network [15,26], thereby compressing interfacial pores and enhancing the mechanical interlocking between fibers and the matrix. As observed in Fig. 21(c), $Ca(OH)_2$ crystals and AFt are interwoven within the matrix, indicating that 4% CMEA continues to provide chemical compensation and alkalinity buffering, while its hydration products effectively fill internal pores. However, PF is a low-modulus fiber whose primary advantage lies in mitigating early-age shrinkage cracking [14], whereas its resistance to tensile stresses at later stages is relatively limited [15,66]. With increasing sulfate DWs, the continuous accumulation of Na_2SO_4 crystallization pressure induces microcrack formation. In contrast, Fig. 21(e) shows that BF surfaces are covered with abundant C-S-H gel and hydration products. Although minor microcracks are present in the surrounding regions, the transverse bridging effect of BF effectively restrains crack opening [14,63], confining $Na_2SO_4{\cdot}10\ H_2O$ crystals within limited space, thereby preventing the formation of a connected crack network.

However, excessive CMEA content (8%) leads to intensified microstructural damage, indicating that overexpansion offsets the beneficial effects of phase regulation. As shown in Fig. 21(f) and Fig. 21(i), excessive hydration of CMEA induces substantial self-expansion stress [21,22], which not only exceeds the mechanical confinement capacity of the fiber network but also superimposes with the crystallization pressure of $Na_2SO_4{\cdot}10\ H_2O$ at later stages. This combined effect results in accelerated deterioration of the matrix. In Fig. 21(f), pronounced interfacial cracks are observed between BF and the matrix, while in Fig. 21(i), these cracks are densely filled with $Na_2SO_4{\cdot}10\ H_2O$ crystals and AFt. The excessive dosage of CMEA disrupts the originally dense ITZ structure [26,27]; instead of providing a beneficial densification effect, it creates internal transport pathways for SO_4^{2-}, thereby accelerating damage evolution.

3.7. Mechanisms governing the resistance of FERC to sulfate DWs

3.7.1. Evolution of SA under DWs

The performance evolution of concrete under sulfate DWs is fundamentally governed by the dynamic competition among ion transport, solid-phase formation, and pore-crack network reconstruction [14,67]. The extent of damage is determined not simply by the amounts of AFt, gypsum, or salt crystals formed, but by the balance between the volume of newly formed solids, the available pore accommodation capacity, and the restraint provided by the matrix [64]. When the reaction and crystallization products can still be accommodated within the original pores, solid-phase formation mainly produces a filling and densification effect. As the available pore space is progressively exhausted, the confined growth of these solids generates localized expansive stresses. Once the accumulated stresses exceed the tensile and fracture resistance of the matrix, microcracks propagate and reconstruct the transport pathways for aggressive species. Based on this competition, the damage process illustrated in Fig. 22 can be divided into four successive stages: pore filling, confined accumulation, stress-induced cracking, and crack-mediated feedback [59].

At the initial stage of exposure, external SO_4^{2-} enters the matrix through capillary absorption and migrates inward through capillary pores, ITZ, and pre-existing microcracks. It reacts with $Ca(OH)_2$ and aluminate hydrates to form gypsum and AFt [59,60]. The XRD and FTIR results obtained after 50 cycles confirmed the presence of AFt and gypsum, together with vibrational features associated with SO_4^{2-}, Al-O, and bound water. However, these end-point measurements identify the types of reaction products present and do not directly indicate their formation rates during the early cycles. During the first 10 cycles, the limited amounts of sulfate reaction products and products of continued hydration

preferentially precipitated within the original pores and interfacial defects. This reduced the effective pore size, pore connectivity,

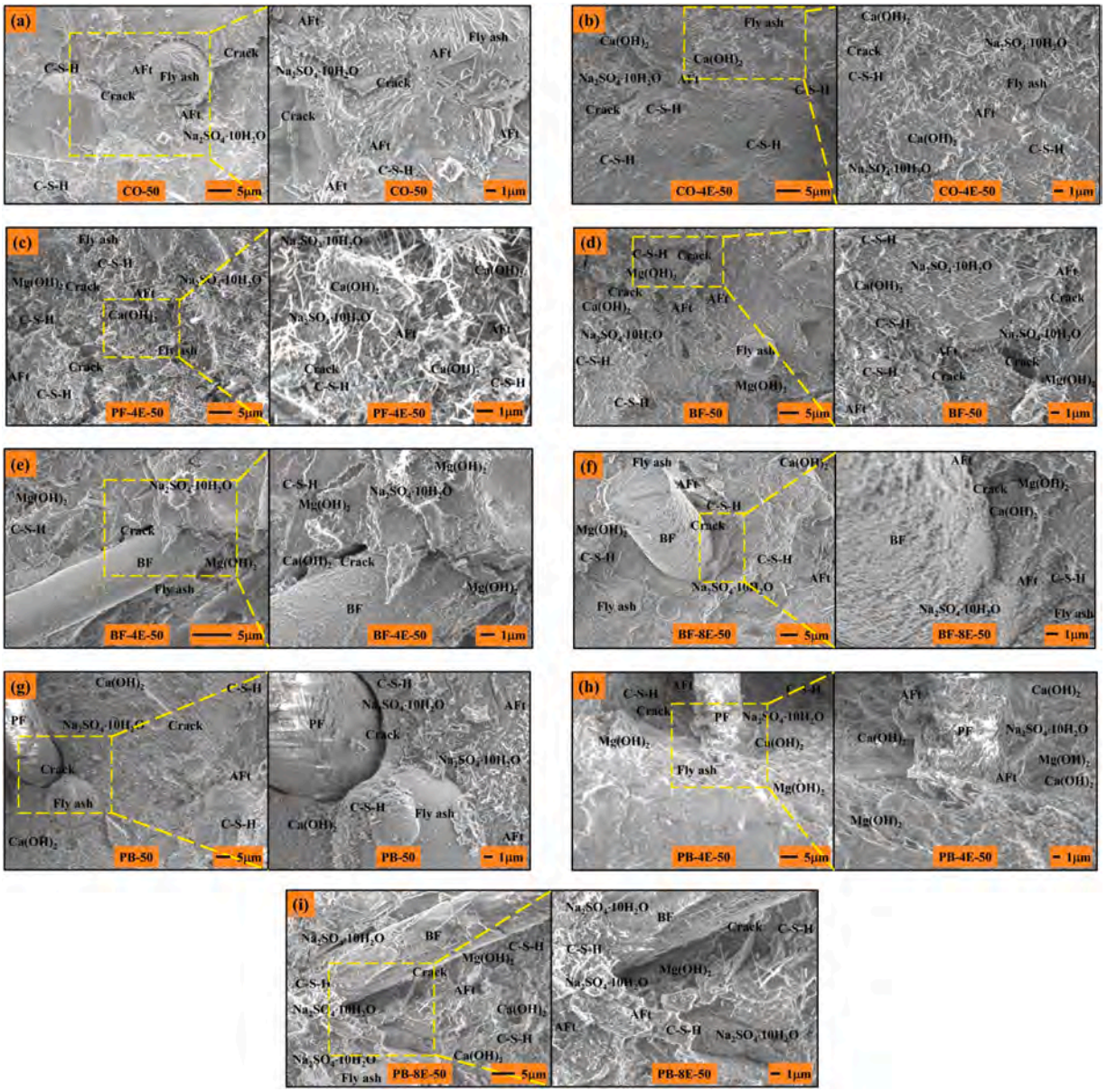

Fig. 21. SEM morphology of FERC under different sulfate DWs times.

and cross-sectional area available for liquid-phase transport. This interpretation is consistent with the concurrent decrease in total porosity, increases in strength and mass, and increases in ER and R_1 during the early stage. These changes indicate that the volume of newly formed solids had not yet exceeded the pore accommodation capacity of the matrix and that the filling effect remained dominant [14]. Because R_1 is governed by both the geometry of the pore network and the conductivity of the pore solution, its initial increase should be interpreted as a coupled response to pore-structure densification and changes in the ionic composition of the liquid phase, rather than as the result of a single transformation between conductive pathways.

With the continued ingress of SO_4^{2-}, the accumulation of AFt, gypsum, and sodium sulfate phases within the limited pore space gradually changes solid-phase formation from unconstrained pore filling to confined growth [64]. The phases formed by Na_2SO_4 in the pores are jointly governed by temperature, relative humidity, water activity, pore-solution composition, and pore-size confinement. In the binary Na_2SO_4-H_2O system, approximately 32.4℃ is the three-phase equilibrium temperature at which anhydrous Na_2SO_4, Na_2SO_4·10 H_2O, and the saturated solution coexist. It should not be regarded as a fixed hydration-transition temperature independent of humidity and solution composition. Below this temperature and at high water activity, Na_2SO_4·10 H_2O is thermodynamically more stable. At lower relative humidity, however, anhydrous Na_2SO_4 may remain the stable salt phase. Above 32.4℃, the stable solid phase in equilibrium with the solution is predominantly anhydrous Na_2SO_4[68]. The pore solution of cement-based materials contains

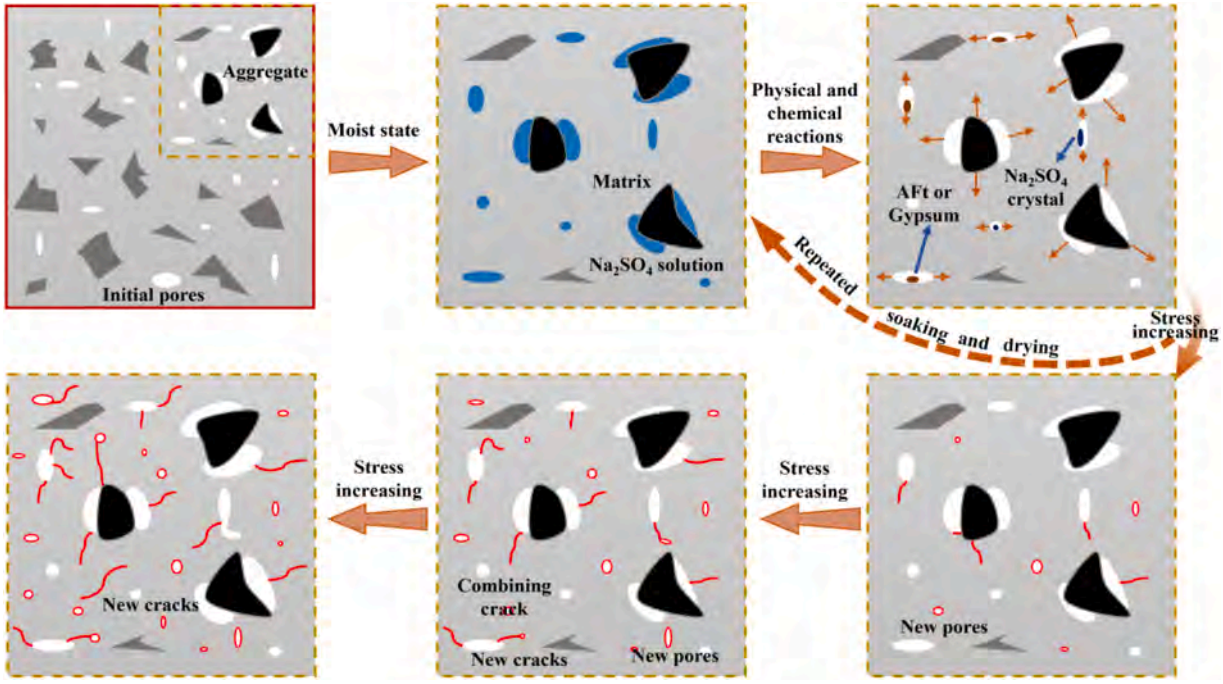

Fig. 22. Schematic illustration of internal damage mechanism of concrete under sulfate DWs.

multiple ionic species and is confined within pores of limited size. Consequently, the actual phase boundaries may deviate from those of the ideal binary system, and the salt phase present in the pores cannot be determined from temperature alone. Under the cycling regime adopted in this study, drying at 60℃ promotes pore-water evaporation and solution concentration, thermodynamically favoring the precipitation of anhydrous Na_2SO_4. During subsequent cooling to room temperature and re-immersion, the residual anhydrous salt dissolves, potentially generating a high local supersaturation with respect to $Na_2SO_4{\cdot}10\ H_2O$. When the local temperature, water activity, and solution composition enter the stable or metastable precipitation region of the decahydrate phase, $Na_2SO_4{\cdot}10\ H_2O$ may nucleate and grow within the confined pore space [69,70].

The direct driving force for physical SA by sodium sulfate is the crystallization pressure generated by crystal growth from a supersaturated solution within confined pores [65,71]. Its magnitude depends on the degree of supersaturation, pore saturation, crystal growth location, and matrix restraint, and therefore cannot be calculated directly from the difference in molar volume between anhydrous Na_2SO_4 and $Na_2SO_4{\cdot}10\ H_2O$ [64]. Meanwhile, the confined formation of AFt and gypsum produces CE [72]. Physical crystallization and chemical reactions compete for the same pore space and interact

by altering pore size, moisture state, and ion-transport conditions [14]. Once the volume of newly formed solids exceeds the available pore accommodation capacity, localized tensile stresses at pore walls and ITZ promote microcrack initiation [73]. Subsequent crack propagation increases liquid-phase connectivity and the accessibility of reactive interfaces, thereby reducing resistance to the inward transport of SO_4^{2-}. This establishes a positive feedback cycle involving solid-phase accumulation, stress-induced cracking,

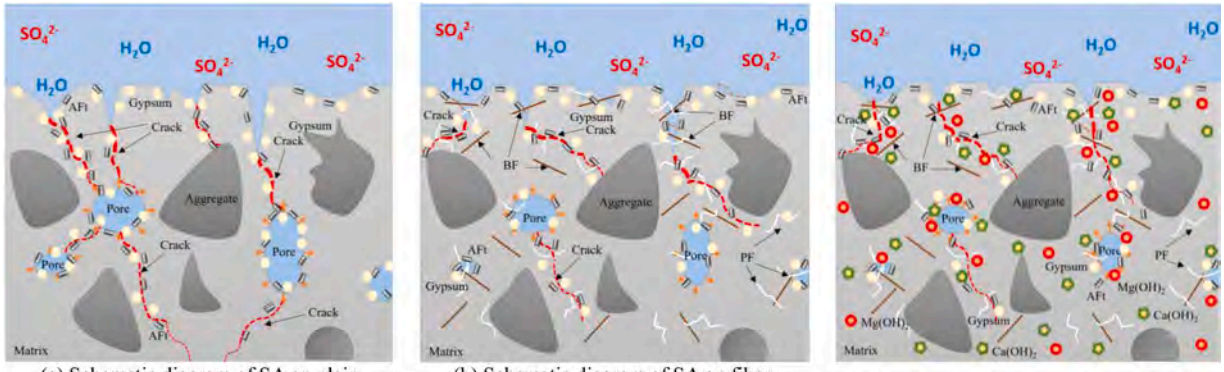

(a) Schematic diagram of SA on plain concrete

(b) Schematic diagram of SA on fiber-reinforced concrete

(c) Schematic diagram of SA on FERC

Fig. 23. Schematic diagram of SA on FERC.

enhanced transport, and accelerated reaction. During the intermediate and later stages, the increases in porosity and the proportion of coarse pores, the nonlinear progression of the sulfate penetration depth, and the decreases in ER, R_1, and R_{ct} collectively indicate that the dominant mechanism shifts from pore filling to crack interconnection. Ultimately, the formation of a connected crack network disrupts the effective load-bearing skeleton, leading to surface spalling, ML, and strength degradation.

3.7.2. Synergistic mechanisms of fibers and CMEA in enhancing sulfate resistance

The synergy between fibers and CMEA is not a simple additive effect. Instead, their combined regulation of solid-phase formation, ion transport, and structural restraint alters the critical conditions governing the transition from pore filling to cracking. The $Ca(OH)_2$ and $Mg(OH)_2$ generated by CMEA hydration can, at an appropriate dosage, fill capillary pores and defects in the ITZ [15], thereby reducing the effective connectivity of the initial transport pathways. Fibers increase resistance to crack propagation through crack bridging, interfacial bonding, and pull-out energy dissipation [14]. CMEA primarily limits the accessibility of SO_4^{2-} and the formation of sulfate-bearing products at greater depths, whereas the fibers enhance the capacity of the matrix to resist and dissipate localized expansive stresses [25]. Their combined action therefore delays the critical transition from pore-filling solid formation to expansion-induced cracking Fig. 23.

The normalized semi-quantitative XRD results show that, after incorporating 4% CMEA into the BF and PB systems, the combined relative proportions of AFt and gypsum among the selected crystalline phases decreased from 50.1% and 53.4–41.4% and 44.3%, respectively. Meanwhile, the relative proportions of $Ca(OH)_2$ and $Mg(OH)_2$ increased. When considered together with the lower SO_4^{2-} penetration, refined PS, and better-preserved ITZ, these results suggest that 4% CMEA reduced the ingress of external sulfate and limited the conditions favorable for the formation of secondary sulfate-bearing products within the matrix. The absence of additional major FTIR absorption bands further indicates that the fibers and CMEA did not alter the principal types of sulfate reaction products. Instead, they modified the relative distribution of the existing phases by regulating sulfate transport and the extent of reaction.

The primary contribution of the fibers occurs during the mechanical stage of damage evolution [14]. Owing to its relatively low E and high ultimate elongation, PF can redistribute localized tensile strains through fiber deformation and interfacial slip when cracks remain small [74]. In contrast, BF has a higher E and TS and therefore provides stronger bridging restraint as cracks propagate [25,75]. Consequently, BF-4E exhibited better pore-structure stability, greater retention of ER, and a higher compressive strength retention ratio. PB-4E achieved a more balanced performance in STS and spalling resistance through the complementary deformation capacity of PF and bridging stiffness of BF. These results indicate that the advantages of different fiber systems arise from their distinct restraint mechanisms at different crack scales rather than from any direct alteration of the types of sulfate reaction products.

CMEA and the fibers also produce mutually reinforcing effects at the interface. The deposition of CMEA hydration products around the fibers and within the ITZ can fill interfacial defects, thereby improving effective fiber bonding and stress transfer [15]. The fiber network restrains the conversion of CMEA-induced volumetric deformation into crack opening [25,26]. Consequently, part of the newly formed solid phase continues to contribute to pore filling rather than directly generating crack-inducing stresses. The hydration products attached to the fiber surfaces and the relatively intact ITZs observed by SEM in BF-4E and PB-4E are consistent with this restrained-deformation mechanism. Crack restraint helps preserve a PS with low connectivity and further slows SO_4^{2-} ingress [14]. The resulting reduction in sulfate ingress, in turn, limits the subsequent confined accumulation of sulfate-bearing products. This interaction establishes a beneficial feedback mechanism involving interfacial densification, reduced transport, limited expansion, and controlled cracking [32,35,76]. The lower total porosity, proportion of harmful pores, and fractal dimension of BF-4E after 50 cycles, together with its higher ER and impedance parameters, reflect the combined effects of this multiscale feedback mechanism. However, this synergy exhibits a distinct dosage-dependent threshold. Although CMEA can improve the PS through the formation of hydration products, it also introduces additional SO_3 and increases the volume of internally generated solids. At a CMEA dosage of 4%, the filling effect of the hydration products remains compatible with the restraint capacity of the fiber network, and solid-phase formation does not exceed the effective accommodation capacity of the system. When the dosage is increased to 8%, the net increase in SO_3 equivalent introduced by CMEA relative to CO rises from 2.03 to 4.06 kg/m^3. Simultaneously, the volume of solids generated by CaO and MgO hydration increases further. Under these conditions, the rate and volume of internal solid-phase formation may exceed the accommodation capacity of the available pore space and the restraining capacity of the fiber network, causing the role of CMEA to shift from defect filling to expansion-induced damage.

After 50 cycles, the normalized combined proportions of AFt and gypsum increased to 57.8% in BF-8E and 62.0% in PB-8E. These increases were accompanied by lower relative proportions of $Ca(OH)_2$ and higher proportions of $Mg(OH)_2$. Although the present XRD results cannot distinguish whether the SO_4^{2-} in the sulfate-bearing phases originated from internal or external sources, these phase changes are consistent with the greater SO_3 input in the mixtures containing 8% CMEA, the interfacial cracks observed by SEM, enhanced SO_4^{2-} transport, and the deterioration in macroscopic performance. The underlying deterioration mechanism can be described as follows. Excessive CMEA increases both internal solid-phase formation and the internal inventory of sulfate-bearing constituents, while the resulting localized volumetric deformation initiates cracking. These cracks subsequently facilitate the ingress of external SO_4^{2-} and accelerate the continued formation of AFt and gypsum. A destabilizing feedback loop is thereby established among internal expansion, crack interconnection, external sulfate ingress, and renewed accumulation of sulfate-bearing products. The performance deterioration of the mixtures containing 8% CMEA is therefore not governed by a single expansive product, but results from the combined effects of internal component reactions, external sulfate ingress, and the loss of effective restraint provided by the fiber network.

The resistance of FERC to sulfate DWs is therefore governed by the dynamic balance among the volume of newly formed solids, the available pore accommodation capacity, and the ability to restrain crack development. At an appropriate dosage, CMEA reduces the accessibility of SO_4^{2-} by filling pores and interfacial defects, while the fibers increase the tolerance of the matrix to expansive

deformation through multiscale crack bridging [25,77]. Their combined action delays the critical transition from filling-induced densification to expansion-induced cracking. Once the CMEA dosage exceeds the spatial accommodation and mechanical restraint capacities of the system, the beneficial feedback mechanism shifts to a destabilizing cycle in which expansion, cracking, and transport mutually reinforce one another [15]. This threshold-dependent coupling mechanism provides a unified explanation for the improved performance of the systems containing 4% CMEA, the later-stage deterioration of those containing 8% CMEA, and the distinct advantages of BF-4E and PB-4E across different durability indicators.

4. Mechanical modeling and equivalent critical-cycle estimation under accelerated sulfate DWs

4.1. Mechanical model of FERC in sulfate environment

4.1.1. Ideal elastic-brittle constitutive model of uncorroded FERC

The constitutive response of uncorroded FERC under uniaxial compression and splitting tension can be interpreted within the framework of the parallel bar model originally developed by Krajcinovic[78]. The physical representation of this model is shown in Fig. 24. In this model, FERC is regarded as a macroscopically homogeneous material. Under external loading, the internal stress state follows classical elasticity theory [79], in which the material is subjected to axial compressive stress f_{cs} and transverse tensile stress f_{ts}. Accordingly, the initial effective load-bearing area of the intact specimen can be defined. The FERC specimen is idealized as a system consisting of N parallel bars with identical cross-sectional area $S$and identical critical fracture stresses (σ_{cs} or σ_{ts}). Accordingly, the initial total effective cross-sectional area of the uncorroded specimen is given by:

$$A = N \bullet S \tag{15}$$

Assuming ideal elastic-brittle behavior, failure is triggered once the applied stress reaches the critical strength of the load-carrying elements, allowing the CS and STS of uncorroded FERC to be analytically expressed.

$$f_{cs}(0) = N \bullet \sigma_{cs} \tag{16}$$

$$f_{ts}(0) = N \bullet \sigma_{ts} \tag{17}$$

4.1.2. Mechanical model considering corrosion effects

SA under DWs evolves as a non-steady diffusion process progressing from the exposed surface toward the interior. Along the penetration direction, the material can be conceptually partitioned into three zones: a deteriorated layer, a densified layer, and an unaffected core [78,80], as illustrated in Fig. 25. The penetration depth is denoted as $x_u(t)$. At early exposure stages, pore filling by reaction products results in local densification. With continued deterioration, internal expansion exceeds the tensile deformation capacity of the matrix, leading to cracking and the development of a damaged region with thickness x_p. To capture these effects, a corrosion damage factor γ_p and a densification enhancement factor γ_u are introduced, and the corresponding effective load-bearing areas of each layer are defined.

$$A_p = T \bullet S \tag{18}$$

$$A_u = U \bullet S \tag{19}$$

Accordingly, the time-dependent CS and STS of FERC are expressed as:

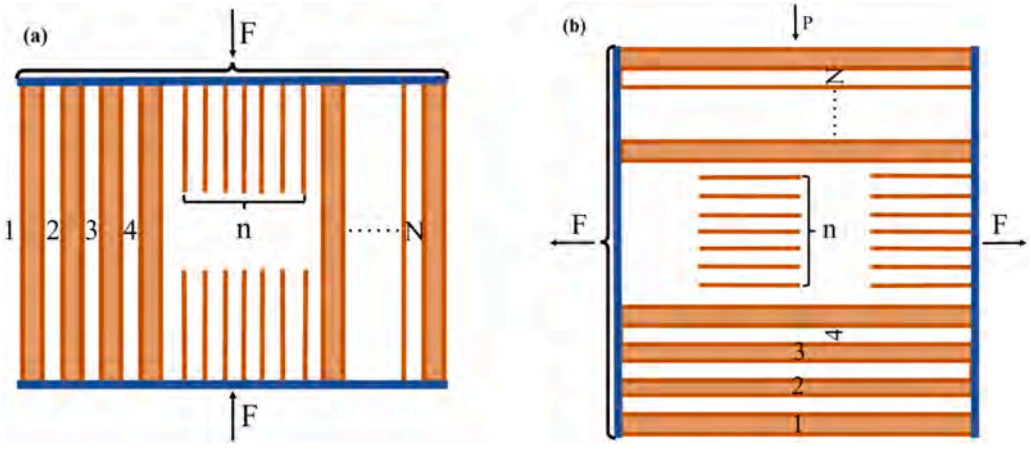

Fig. 24. Parallel bar model for uncorroded FERC.

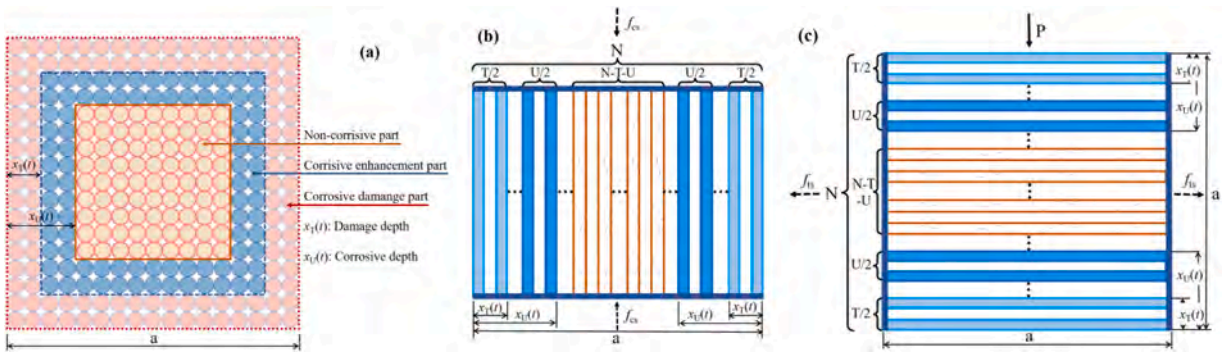

Fig. 25. Mechanical models of CS and STS considering corrosion effects ((a) Corrosion effect; (b) Uniaxial compression parallel bar system; (c) Splitting tensile parallel bar system).

$$f_{cs}(t) = (N-T-U)\bullet\sigma_{cs} + T\bullet\sigma_{ct} + U\bullet\sigma_{cu} = \left(\frac{N-T-U}{N} + \gamma_{cp}\bullet\frac{T}{N} + \gamma_{cu}\bullet\frac{T}{U}\right)\bullet f_{cs}(0)$$

$$= \left[1 - \left(1-\gamma_{cp}\right)\bullet\frac{a^2 - \left(a-2\bullet x_p(t)\right)^2}{a^2} - (1-\gamma_{cu})\bullet\frac{\left(a-2\bullet x_p(t)\right)^2 - \left(a-2\bullet x_u(t)\right)^2}{a^2}\right]\bullet f_{cs}(0) \tag{20}$$

$$f_{ts}(t) = (N-T-U)\bullet\sigma_{ts} + T\bullet\sigma_{tt} + U\bullet\sigma_{tu} = \left(\frac{N-T-U}{N} + \gamma_{tp}\bullet\frac{T}{N} + \gamma_{tu}\bullet\frac{T}{U}\right)\bullet f_{ts}(0)$$

$$= \left[1 - \left(1-\gamma_{tp}\right)\bullet\frac{a^2 - \left(a-2\bullet x_p(t)\right)^2}{a^2} - (1-\gamma_{tu})\bullet\frac{\left(a-2\bullet x_p(t)\right)^2 - \left(a-2\bullet x_u(t)\right)^2}{a^2}\right]\bullet f_{ts}(0) \tag{21}$$

where $f_{cs}(t)$ and $f_{ts}(t)$ are the CS and STS at time t.

4.1.3. Determination of damage depth (DP) and critical ion concentration

The transport of SO_4^{2-} in FERC follows a non-steady diffusion process [14]. Considering long-term environmental exposure, a time-dependent diffusion coefficient is adopted based on Thomas' model [78,81]:

$$D(t) = D_0 \bullet \left(\frac{t}{t_0}\right)^k \tag{22}$$

Where $D(t)$ denotes the time-dependent apparent diffusion coefficient of SO_4^{2-} species during the progressive densification stage of FERC; D_0 corresponds to the reference diffusivity at an initial instant t_0; and k represents the temporal decay exponent governing the evolution of SO_4^{2-} diffusivity.

Assuming a semi-infinite medium [78], the sulfate concentration distribution along depth can be expressed as:

$$C_f(x,t) = C_0 + (C_S - C_0)\bullet erfc\left(\frac{x}{2\sqrt{\left[D_0\bullet\left(\frac{t}{t_0}\right)^k\right]\bullet t}}\right)$$

$$= C_0 + (C_S - C_0)\bullet erfc\left(\frac{x}{2\sqrt{D(t)\bullet t}}\right) \tag{23}$$

Thus, the critical DP $x_p$can be obtained by:

$$x_p = 2\bullet\sqrt{(D(t)\bullet t)}\bullet erfc^{-1}\left(\frac{C_f(x_p,t) - C_0}{C_S - C_0}\right) \tag{24}$$

Where x_p is the critical DP of FERC after SA; $erfcinv(x)$ is the inverse function of the complementary error function; $C_f(x_p,t)$ is the critical state SO_4^{2-} concentration corresponding to the critical concentration.

4.1.4. Physico-chemical coupled criterion for critical concentration $C_f(x_p, t)$

Under DWs conditions, degradation of FERC is driven by the combined effects of crystallization-induced physical stress and chemically induced expansion. The former arises from the crystallization of Na_2SO_4 during moisture fluctuations, while the latter originates from reactions between SO_4^{2-} and hydration products, producing expansive phases such as gypsum and AFt. Previous studies have indicated that the dominant damage under DWs occurs during the wetting stage [81]. Specifically, anhydrous sodium sulfate (Na_2SO_4) formed during the drying phase dissolves upon rewetting, generating a supersaturated $Na_2SO_4{\cdot}10\ H_2O$ solution that subsequently precipitates, accompanied by significant volumetric expansion. According to porous media mechanics and composite material theory, the volumetric strain induced by salt crystallization can be expressed as [80]:

$$\varepsilon_p = \frac{bp_l + b_c \frac{RT}{V_m} \ln\beta}{K} \tag{25}$$

where ε_p is the crystallization-induced volumetric strain; p_l is the hydrostatic pressure exerted by the pore solution (Pa); V_m denotes the molar volume of $Na_2SO_4{\cdot}10\ H_2O$ (m^3/mol); b_c is the generalized Biot coefficient associated with $Na_2SO_4{\cdot}10\ H_2O$ crystallization; K represents the bulk modulus of the composite (GPa); b is the generalized Biot coefficient;; and β is the supersaturation ratio.

The volumetric strain induced by chemical reactions, mainly due to AFt formation, is given by [80]:

$$\varepsilon_c = \alpha_s CA^{react} \tag{26}$$

where ε_c is the CE strain, CA^{react} is the consumed aluminate concentration (m^3/mol), and α_s is a coefficient determined by the fraction of reactive aluminate phases in the system.

Before the expansive products fill the initial pore space, their formation primarily contributes to pore filling and produces only limited effective expansion of the matrix. As the available pore space is progressively exhausted, subsequently formed crystallization and chemical reaction products begin to exert expansive stresses on the pore walls. The critical and cracking states are defined using the following strain criteria [78,80]:

Critical concentration condition:

$$\frac{1}{3}\varepsilon_v = 0 \tag{27}$$

Cracking concentration condition:

$$\frac{1}{3}\varepsilon_v = \varepsilon_t \tag{28}$$

where ε_v is the effective volumetric expansion strain induced by the coupled physical and chemical actions, and ε_t is the ultimate tensile strain of the FERC.

Because the supersaturation ratio β is jointly affected by the number of cycles, moisture transport, and pore-structure evolution, the present experiments cannot separately quantify the expansion strains induced by physical salt crystallization and chemical reactions. To enable quantitative determination of the critical damage state, the baseline calculation follows an existing model and assumes that the sulfate concentrations associated with the physical and chemical processes are equal. At the same sulfate concentration, the

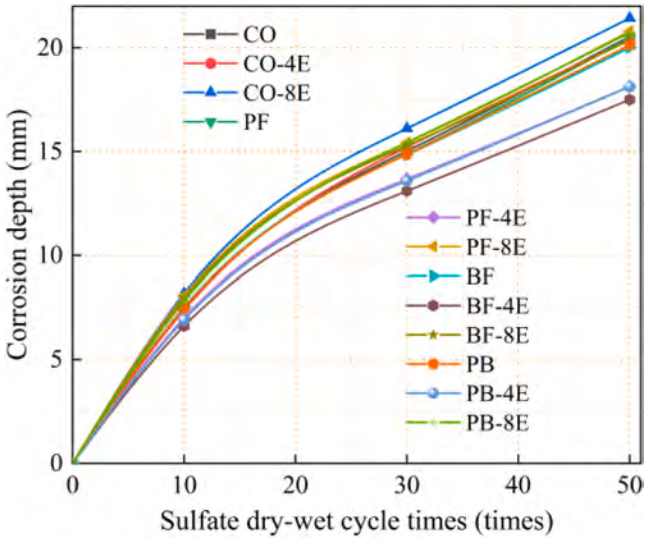

Fig. 26. Evolution of damage layer thickness under different sulfate DWs.

physical crystallization strain is assumed to be twice the CE strain [73,81,82]. This relationship is a simplifying assumption introduced for model closure rather than a universal material constant.

To evaluate the influence of the assumed independent linear superposition of physical crystallization strain and CE strain on the calculated results, a dimensionless sensitivity coefficient λ is introduced into the physical crystallization strain term. The total effective expansion strain is then expressed as [80]:

$$\varepsilon_v = \varepsilon_c + \lambda\varepsilon_p - f\varphi_0 \tag{29}$$

where $f\varphi_0$ represents the effective accommodation capacity of the initial pores for expansive products, and λ is the sensitivity coefficient for the contribution of physical crystallization. A value of $\lambda = 1.00$ corresponds to the independent linear superposition assumed in the original model. A value of $\lambda < 1.00$ indicates that the effective contribution of physical crystallization strain is reduced by processes such as pore filling or competition between reactions, whereas $\lambda > 1.00$ indicates that crack propagation and the reorganization of transport pathways may amplify the effect of physical crystallization. Local sensitivity analysis was performed using λ values of 0.75, 1.00, and 1.25, corresponding to effective physical-to-CE strain ratios of 1.5, 2.0, and 2.5, respectively. All other model parameters were held constant.

Based on the cement composition reported in Table 1 and the mixture proportions given in Table 7, the initial tricalcium aluminate (C_3A) content per unit volume of concrete was calculated as 91.63 mol/m^3 . The values of $f\varphi_0$, α_s, q, and the ultimate tensile strain of concrete ε_t were taken as 0.0079, 2.75×10^{-4}m^3/mol, 2.6, and 1.5×10^{-4}, respectively. Under the baseline condition (λ=1.00), Eqs. (26)-(29) yielded a critical SO_4^{2-} mass fraction of 1.085%. Substituting this critical concentration into Eq. (24) and combining it with the measured SO_4^{2-} concentration profiles along the depth direction allowed the damage-layer thickness (DLT) to be determined at different numbers of cycles. As shown in Fig. 26, the DLT increased continuously with the number of DWs, indicating that both the penetration front and the damaged region progressively advanced into the concrete.

Starting from the baseline physical crystallization-to-CE strain ratio of 2.0, λ was set to 0.75, 1.00, and 1.25, corresponding to effective physical-to-CE strain ratios of 1.5, 2.0, and 2.5, respectively. Because $\varepsilon_p = 2\varepsilon_c$ in the baseline model, the variation in the critical concentration with λ can be expressed as:

$$C_f(\lambda) = 1.085\% \times \frac{3}{1 + 2\lambda} \tag{30}$$

where 1.085% is the critical SO_4^{2-} mass fraction obtained from the baseline model at $\lambda = 1.00$. For λ values of 0.75, 1.00, and 1.25, the corresponding effective physical-to-CE strain ratios are 1.5, 2.0, and 2.5, respectively, and the calculated critical SO_4^{2-} mass fractions are 1.302%, 1.085%, and 0.930%. These critical concentrations were substituted separately into Eq. (24). The DLT were then calculated using the fitted SO_4^{2-} concentration-depth profiles of CO, BF-4E, and PB-4E after 50 cycles. The results are presented in Table 9.

As shown in Table 9, variations in the contribution of physical crystallization affect the DLT through the critical concentration criterion. When λ decreased from 1.00 to 0.75, the effective physical-to-CE strain ratio decreased from 2.0 to 1.5, while the critical SO_4^{2-} mass fraction increased from 1.085% to 1.302%. Consequently, the DLT of CO, BF-4E, and PB-4E decreased by 8.67%, 7.27%, and 5.64%, respectively. When λ increased from 1.00 to 1.25, the effective strain ratio increased to 2.5 and the critical concentration decreased to 0.930%. The corresponding DLT increased by 15.68%, 13.65%, and 15.91%, respectively. The asymmetric response of the DLT to increases and decreases in λ is mainly attributable to the nonlinear SO_4^{2-} concentration gradient along the penetration depth [14,78]. Therefore, a change in the critical concentration does not produce a proportional displacement of the penetration front.

Although variations in λ affect the absolute calculated values of the critical concentration and DLT, the DLT consistently followed the order BF-4E<PB-4E<CO over the investigated range of 0.75–1.25. Thus, the relative ranking of sulfate resistance remained unchanged. This finding indicates that the physical-chemical coupling assumption primarily affects the quantitative estimation of damage severity but does not alter the durability assessment of the fiber-CMEA systems relative to the reference concrete. The model therefore exhibits a degree of robustness in comparing different material systems. Nevertheless, the absolute predictions of DLT and subsequent service life should be regarded as conditional estimates applicable to the specified parameter values and experimental exposure regime.

Based on the above analysis, $\lambda = 1.00$ was adopted as the baseline condition in the subsequent calculations, corresponding to an effective physical crystallization-to-CE strain ratio of 2.0. The cases of $\lambda = 0.75$ and 1.25 were used to characterize the range of variation in the calculated results arising from this simplifying assumption.

4.1.5. Model validation and analysis

By substituting Eqs. (3) and (24) into Eqs. (20) and (21), the predictive formulations for the CS and STS of FERC under different

Table 9
Effect of the physical-chemical strain sensitivity coefficient on the critical concentration and DLT after 50 cycles.

λ	Effective physical-to-CE strain ratio	Critical SO_4^{2-} mass fraction (%)	DLT of CO (mm)	DLT of BF-4E (mm)	DLT of PB-4E (mm)
0.75	1.5	1.302	17.59	15.56	15.89
1.00	2.0	1.085	19.26	16.78	16.84
1.25	2.5	0.930	22.28	19.07	19.52

sulfate DWs can be obtained as follows:

$$\begin{cases} f_{cs}(t) = \left[1 - \left(1 - \gamma_{cp}\right) \bullet \dfrac{a^2 - \left(a - 2 \bullet x_p(t)\right)^2}{a^2} - (1 - \gamma_{cu}) \bullet \dfrac{\left(a - 2 \bullet x_p(t)\right)^2 - \left(a - 2 \bullet x_u(t)\right)^2}{a^2}\right] \bullet f_{cs}(0) \\ x_p(t) = k_p \bullet t^{\alpha} \\ x_u(t) = 2\sqrt{\left[D \bullet \left(\dfrac{t}{t_0}\right)^k\right] t} \bullet erfc^{-1}\left(\dfrac{C(x,t) - C_0}{C_S - C_0}\right) \end{cases} \tag{31}$$

$$\begin{cases} f_{ts}(t) = \left[1 - \left(1 - \gamma_{tp}\right) \bullet \dfrac{a^2 - \left(a - 2 \bullet x_p(t)\right)^2}{a^2} - (1 - \gamma_{tu}) \bullet \dfrac{\left(a - 2 \bullet x_p(t)\right)^2 - \left(a - 2 \bullet x_u(t)\right)^2}{a^2}\right] \bullet f_{ts}(0) \\ x_p(t) = k_p \bullet t^{\alpha} \\ x_u(t) = 2\sqrt{\left[D \bullet \left(\dfrac{t}{t_0}\right)^k\right] t} \bullet erfc^{-1}\left(\dfrac{C(x,t) - C_0}{C_S - C_0}\right) \end{cases} \tag{32}$$

Fig. 27 compares the calculated and measured compressive and STS. Within the calibrated 0–50-cycle dataset, the model reproduced the nonlinear strength evolution, with R^2 values above 0.96 for both responses. This agreement indicates that the layered chemo-mechanical model can describe the strength evolution under the adopted accelerated exposure conditions; however, its predictive performance beyond the calibration range requires independent validation. At approximately 20 DWCs, differences among the mixtures became more apparent. BF-4E retained 76.26% of its initial CS, whereas the corresponding value for CO-8E decreased to 56.50%, indicating more rapid deterioration of the latter mixture. The calculated results further indicate that the combined use of fibers and an appropriate CMEA dosage delayed the advance of the damaged layer, thereby reducing the loss of effective load-bearing area.

4.2. Estimation of the equivalent critical number of cycles for FERC under accelerated sulfate DWs

Under sulfate DWs, SO_4^{2-} progressively migrates into the concrete and drives the damaged region deeper through salt crystallization and chemical reactions. To quantitatively compare the ability of different material systems to delay the advance of the penetration front, the number of cycles required for the DLT to reach a prescribed critical value is defined as the equivalent critical number of cycles, t_s. This indicator characterizes the relative durability of different mixtures under the same accelerated exposure regime and should not be interpreted as a deterministic service life under actual engineering conditions.

An equivalent critical-cycle prediction model was developed based on the analytical solution to Fick's second law for one-dimensional, non-steady-state diffusion [78,83]. Microcracking and strength degradation are assumed to initiate when the internal ion concentration reaches the critical concentration $C_f(x_p,t)$. By inverting the damage-depth relationship defined in Eq. (24), the equivalent exposure duration ts required to reach the prescribed critical damage depth x_p can be determined. The governing equations are given in Eqs. (33) and (34):

$$t_s = \left(\frac{x_p}{2 \bullet erfc^{-1}\left(\frac{C(x,t) - C_0}{C_S - C_0}\right)}\right)^2 \bullet \frac{1}{D_0} \bullet \left(\frac{t_s}{t_0}\right)^{-k} \tag{33}$$

$$t_s = \left[\left(\frac{x_p^2}{4D_0} \bullet \left(\frac{1}{erfc^{-1}\left(\frac{C(x,t) - C_0}{C_S - C_0}\right)}\right)^2\right) \bullet t_0^k\right]^{\frac{1}{1+k}} \tag{34}$$

Based on the proposed model, the equivalent critical-cycle responses of all mixtures were predicted, as shown in Fig. 28. According to Fig. 28(a), the predicted maximum penetration depth of the reference mixture CO reached 60.43 mm after 280 cycles, indicating severe deterioration of plain concrete under prolonged accelerated exposure. The incorporation of CMEA alone (CO-4E and CO-8E) provided only limited reductions in penetration depth. In contrast, the fiber-reinforced mixtures exhibited greater resistance to sulfate penetration. Without CMEA, the penetration depths of BF and PB were 6.06% and 4.29% lower than that of CO, respectively. When the fibers were combined with 4% CMEA, the predicted penetration depths of BF-4E and PB-4E decreased to 49.34 and 50.58 mm, corresponding to reductions of 18.35% and 16.30%, respectively. Within the investigated dosage range, 4% CMEA provided the most favorable performance. A higher dosage, as represented by PF-8E, reduced sulfate resistance because excessive delayed expansion increased structural defects and loosened the matrix.

Fig. 28(b) presents the model-predicted equivalent critical number of cycles for each mixture at prescribed critical damage depths ranging from 0 to 60 mm. The equivalent critical number of cycles increased nonlinearly with damage depth, and the rate of increase varied markedly among the material systems. At a damage depth of 30 mm, the predicted value for BF-4E was 33.60% higher than that

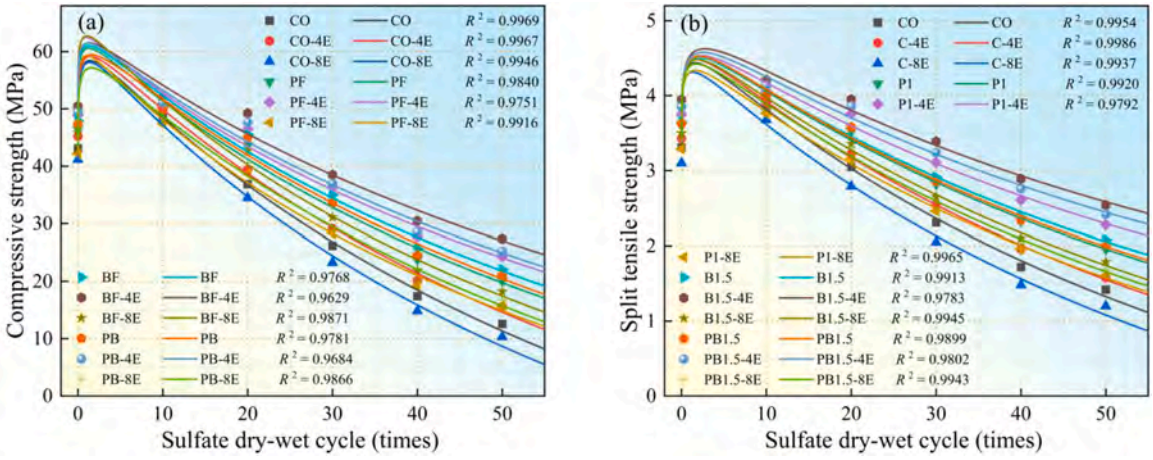

Fig. 27. Comparison between predicted and experimental CS and STS of FERC under SA.

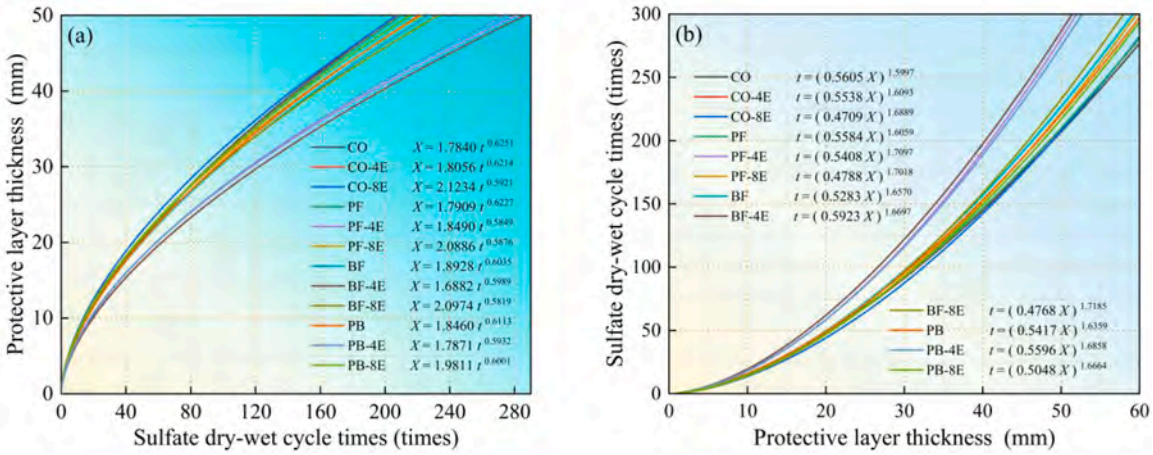

Fig. 28. Model predictions under accelerated sulfate DWCs.

for CO. At 50 mm, this increase reached 38.46%. PB-4E and PF-4E also exhibited higher predicted equivalent critical cycle counts than CO, indicating that the combined use of fibers and an appropriate CMEA dosage can delay the inward progression of the penetration front.

It should be emphasized that these cycle counts were extrapolated from the concentration profiles and damage-depth data obtained within the range of 0–50 cycles and were not directly validated by corresponding long-term cycling tests. Their absolute values are jointly affected by the critical concentration, the assumed relationship between physical and chemical strains, the time-dependent parameters of the diffusion coefficient, the surface concentration, the prescribed damage depth, and the one-dimensional diffusion assumption [4,81,84]. Table 9 further demonstrates that variations in the physical crystallization contribution coefficient λ alter both the critical concentration and the DLT. Accordingly, the results presented in Fig. 28 should be regarded as conditional estimates under the accelerated cycling regime and model assumptions adopted in this study. They are intended primarily for relative comparisons among the investigated material systems. Application of the model to natural sulfate environments, different temperature and humidity regimes, and actual structural scales requires further validation through long-term exposure tests, field monitoring, and appropriate environmental conversion factors.

5. Conclusions

This study elucidated the resistance mechanisms of fiber-CMEA systems under sulfate DWs through analyses of macroscopic performance, ion transport, electrical response, and microstructure. A layered damage model and a method for estimating the equivalent critical number of cycles were also developed. The main conclusions are as follows:

(1) Over 0–50 cycles, all mixtures exhibited early-stage improvement, rapid intermediate-stage deterioration, and a slower decline in the later stage. After 50cycles, BF-4E achieved the best compressive performance, with a compressive strength of 27.36 MPa and a strength retention of 54.17%. PB-4E provided a better balance between tensile resistance and resistance to spalling. Its STS retention was 72.60% after 40 cycles, while its ML rate was only 6.21% after 50 cycles, 34.77% lower than that of CO. When the CMEA dosage increased to 8%, the compressive strength retention of CO-8E decreased to 25.08%, and the ML rate of PB-8E increased to 9.47%. These results indicate that a high CMEA dosage impaired later-stage durability.

(2) SO42- exhibited a non-steady-state distribution that decreased from the specimen surface inward, while the penetration depth increased nonlinearly with the number of cycles. After 50 cycles, the penetration depth in CO exceeded 26 mm, and its surface SO_4^{2-} mass fraction reached 12.77%. The surface SO_4^{2-} mass fractions of the fiber-reinforced mixtures were approximately 10% lower than that of CO, while their penetration depths were also reduced. The coefficients of determination for the time-dependent power-law model were all above 0.97. ER and R1 generally increased initially and then decreased. The early increase in electrical resistance reflected the coupled effects of pore densification and changes in pore-solution ion composition. After 50 cycles, the ER, R1, and Rct of BF-4E were 175.39Ωm, 9350Ω, and 23,898Ω, respectively, indicating that BF-4E delayed crack interconnection and the re-establishment of low-resistance conductive paths.

(3) The normalized semi-quantitative XRD results showed that, after incorporating 4% CMEA into the BF and PB systems, the combined relative proportions of AFt and gypsum decreased from 50.1% and 53.4–41.4% and 44.3%, respectively. When the CMEA dosage increased to 8%, these proportions rose to 57.8% and 62.0%, respectively. Compared with CO, 4% and 8% CMEA introduced net increases in SO3 equivalent of 2.03 and 4.06 kg/m3, respectively, while FTIR revealed no new major chemical bonding features. After 50 cycles, BF-4E had a total porosity of 3.86%, 14.79% lower than that of CO. Its proportions of harmless and harmful pores were 53.14% and 4.21%, respectively, and its pore-structure fractal dimension was 2.61. Together with the SEM observations, these results indicate that an appropriate CMEA dosage reduced SO42- accessibility by filling pores and ITZ defects, while the fibers restrained crack propagation through multiscale bridging. Once solid-phase formation exceeded the accommodation capacity of the pores and the restraining capacity of the fibers, the system shifted to an unstable feedback loop in which expansion, cracking, and transport mutually reinforced one another.

(4) The layered damage model reproduced the nonlinear evolution of compressive and splitting tensile strengths, with R2 values above 0.96 for both responses within the calibrated dataset. Under the baseline condition (λ=1.00), the critical SO42- mass fraction was 1.085%. Varying λ from 0.75 to 1.25 changed the absolute values of the critical concentration and DLT, but the sulfate resistance consistently followed the order BF-4E>PB-4E>CO. At a prescribed damage depth of 30 mm, the equivalent critical cycle counts for CO and BF-4E were 91.38 and 122.08 cycles, respectively, representing an increase of 33.60% for BF-4E.

The conclusions of this study are based on accelerated tests conducted in a 15% Na_2SO_4 solution using a drying temperature of 60℃, a 24 h cycling protocol, and an exposure range of 0–50 DWCs. The XRD results represent normalized semi-quantitative comparisons of selected crystalline phases without an internal standard. Therefore, they should not be interpreted as absolute phase contents and cannot distinguish between the internal and external sources of SO_4^{2-} in sulfate-bearing phases. The layered damage model assumes one-dimensional, non-steady-state diffusion and an equivalent relationship between physical crystallization strain and chemical expansion strain. Moreover, the equivalent critical cycle counts were extrapolated from data obtained over a limited number of cycles and have not been independently validated through corresponding long-term exposure tests. They should therefore be regarded as conditional estimates for comparing the relative durability of different mixtures under the adopted accelerated exposure regime, rather than as deterministic service lives under actual engineering conditions. Future studies should combine long-term laboratory testing, natural-environment exposure, and field monitoring to further calibrate the coupled physical-chemical-damage parameters, evaluate the effects of sulfate concentration, temperature and humidity regimes, and multi-ion exposure conditions, and establish a validated conversion relationship between accelerated drying-wetting cycles and actual service time.

Funding

This work was supported by the Jiangsu Graduate Research and Practice Innovation Program (No. 26CXJH1475, KYCX25_0940), the Fundamental Research Funds for the Central Universities (No. B250205014), the National Key R&D Program of China (No. 2024YFC3210602), the Joint Key Fund of the National Natural Science Foundation of China-Yalong River (No. U25B20223), the National Natural Science Foundation of China (Nos. 52379123, 52279131, 52279099, and 52109123), the Qinglan Project of Jiangsu Province (2025), and the China Scholarship Council (CSC) (Nos. 202506710073 and 202506710074). The authors also acknowledge the Doctoral Special Program of the Young Sci-Tech Talent Cultivation Project by the China Association for Science and Technology (CAST).

CRediT authorship contribution statement

Lei Gan: Validation, Funding acquisition, Conceptualization. **Giuseppe Lacidogna:** Supervision, Resources, Conceptualization. **Jianqing Tang:** Visualization, Methodology, Data curation. **Yunlin Ma:** Investigation, Formal analysis. **Tong Wang:** Investigation, Data curation. **Yang Lu:** Supervision, Resources, Project administration, Funding acquisition. **Zhenghong Tian:** Supervision, Resources, Project administration, Funding acquisition. **Su Lu:** Writing – original draft, Methodology, Formal analysis, Conceptualization. **Jiaxin Liu:** Writing – review & editing, Funding acquisition, Conceptualization. **Alessandro P. Fantilli:** Writing – review & editing, Supervision, Resources. **Xiao Sun:** Resources, Methodology, Funding acquisition.

Declaration of Competing Interest

The authors declare that they have no known competing financial interests or personal relationships that could have appeared to influence the work reported in this paper.

Data availability

Data will be made available on request.

References

[1] V.G. Cappellesso, J.M. Etcheverry, Y.A. Villagran-Zaccardi, E. Gruyaert, K. Van Tittelboom, N. De Belie, Mitigating sulfate attack in self-healing concrete using bacteria-based or crystalline admixture healing agents, Cem. Concr. Compos. 169 (2026) 106514, https://doi.org/10.1016/j.cemconcomp.2026.106514.

[2] D. Huang, H. Gao, Q. Xia, J. Tian, Y. Li, D. Niu, Effect of low pressure on mechanical properties, microstructure, and durability of concrete: a review, J. Eng. Res. 14 (2) (2026) 1374–1389, https://doi.org/10.1016/j.jer.2025.12.013.

[3] C. Zhang, J. Li, M. Yu, Y. Lu, S. Liu, Mechanism and performance control methods of sulfate attack on concrete: a review, Materials 17 (19) (2024) 4836, https://doi.org/10.3390/ma17194836.

[4] D. Huang, X. Wang, Y. Feng, J. Tian, Y. Li, L. Su, Degradation behavior of early-age frozen mortar under the combined effects of sulfate attack and freeze-thaw cycles, Constr. Build. Mater. 498 (2025) 144028, https://doi.org/10.1016/j.conbuildmat.2025.144028.

[5] Y. Li, Y. Huang, Y. Li, R. Wang, K. Kong, Abrasion resistance and spatial damage gradient of concrete containing different types of coarse aggregates, Constr. Build. Mater. 505 (2025) 144793, https://doi.org/10.1016/j.conbuildmat.2025.144793.

[6] R. Wang, N. Tian, Y. Li, Performance evolution and life prediction of different polymeric coatings for concrete under coupled action of sulfate attack and dry-wet cycles, J. Build. Eng. 119 (2026) 115151, https://doi.org/10.1016/j.jobe.2025.115151.

[7] Y. Li, D. Yan, Y. Li, Y. Zhang, R. Wang, X. Zhuang, J. He, The macro-micro properties of concrete coated with modified polyurethane under the alternating action of abrasion and freeze-thaw cycles, Constr. Build. Mater. 516 (2026) 145705, https://doi.org/10.1016/j.conbuildmat.2026.145705.

[8] R. Wang, Y. Liu, Y. Li, X. Zhuang, Performance degradation mechanism and strength prediction of silica fume concrete under sulfate dry–wet cycles, Case Stud. Constr. Mater. 23 (2025) e05163, https://doi.org/10.1016/j.cscm.2025.e05163.

[9] L. Yan, L. Liu, C. Liu, Bonding performances of polypropylene fiber reinforced concrete beam-type specimen at corrosion conditions: experimental and simulation study, J. Build. Eng. 105 (2025) 112479, https://doi.org/10.1016/j.jobe.2025.112479.

[10] C. Liu, X. Liu, L. Yan, L. Liu, Z. Dong, J. Miao, Bond performance of corroded reinforced concrete subjected to water cooling: experimental study and constitutive modeling with polypropylene fibers, Structures 82 (2025) 110523, https://doi.org/10.1016/j.istruc.2025.110523.

[11] C. Liu, L. Liu, L. Yan, S. Leonovich, J. Miao, Local bond behavior of polypropylene fiber-reinforced concrete based on failure mechanism under transient fire condition: experimental and theoretical research, Constr. Build. Mater. 536 (2026) 146986, https://doi.org/10.1016/j.conbuildmat.2026.146986.

[12] L. Yan, C. Liu, L. Liu, C. Zheng, P. Ba, High-temperature bonding performance and size effect analysis of basalt-polypropylene hybrid fiber-reinforced concrete, Composites Part B Engineering 307 (2025) 112858, https://doi.org/10.1016/j.compositesb.2025.112858.

[13] L. Yan, J. Zhang, S. Wang, Y. Long, Research on the mechanical and bonding properties of steel-polypropylene hybrid fiber reinforced concrete under freeze-thaw-carbonation conditions, J. Build. Eng. 128 (2026) 116635, https://doi.org/10.1016/j.jobe.2026.116635.

[14] S. Lu, J. Liu, Z. Tian, Y. Lu, G. Liang, L. Zhang, H. Bian, Deterioration mechanisms and strength prediction of hybrid fiber-reinforced concrete under coupled sulfate attack and dry-wet cycles, Constr. Build. Mater. 493 (2025) 143243, https://doi.org/10.1016/j.conbuildmat.2025.143243.

[15] S. Lu, J. Liu, Z. Tian, Y. Lu, Z. Li, G. Liang, J. Zhang, Multiscale evaluation and mechanistic insight into the synergistic regulation of early-age volume stability in concrete by hybrid fibers and expansive agent, Constr. Build. Mater. 502 (2025) 144304, https://doi.org/10.1016/j.conbuildmat.2025.144304.

[16] B. Pushpakumara, S. Subawickrama, G.S. De Silva, S.M.S.M. Samarakoon, K.F. Gebremariam, Effect of graphene oxide–treated textile waste cotton and polyester fibers on fresh, mechanical, thermal and durability properties of cement mortar, Constr. Build. Mater. 527 (2026) 146432, https://doi.org/10.1016/j.conbuildmat.2026.146432.

[17] J. Zhuang, S. Shen, Y. Yang, K. Xu, P. Ni, Mechanical performance of basalt and PVA fiber reinforced hybrid-fiber engineered cementitious composite with superimposed basalt fiber content, Constr. Build. Mater. 353 (2022) 129183, https://doi.org/10.1016/j.conbuildmat.2022.129183.

[18] V. Afroughsabet, L. Biolzi, T. Ozbakkaloglu, High-performance fiber-reinforced concrete: a review, J. Mater. Sci. 51 (14) (2016) 6517–6551, https://doi.org/10.1007/s10853-016-9917-4.

[19] Z. Pan, Y. Zhu, D. Zhang, N. Chen, Y. Yang, X. Cai, Effect of expansive agents on the workability, crack resistance and durability of shrinkage-compensating concrete with low contents of fibers, Constr. Build. Mater. 259 (2020) 119768, https://doi.org/10.1016/j.conbuildmat.2020.119768.

[20] C. Li, J. Li, Q. Ren, Q. Zheng, Z. Jiang, Durability of concrete coupled with life cycle assessment: Review and perspective, Cem. Concr. Compos. 139 (2023) 105041, https://doi.org/10.1016/j.cemconcomp.2023.105041.

[21] S. Lu, J. Liu, C. Peng, J. Zhang, H. Sun, Multi-objective optimization of mix proportions for mass concrete with enhanced resistance to cracking and reduced temperature rise, Case Stud. Constr. Mater. 20 (2024) e02810, https://doi.org/10.1016/j.cscm.2023.e02810.

[22] J. Liu, J. Zhang, S. Lu, G. Liang, C. Peng, Multi-scale performance of large-volume concrete under dual control of temperature and deformation, Constr. Build. Mater. 454 (2024) 139116, https://doi.org/10.1016/j.conbuildmat.2024.139116.

[23] L. Liu, Z. Fang, Z. Huang, Y. Wu, Solving shrinkage problem of ultra-high-performance concrete by a combined use of expansive agent, super absorbent polymer, and shrinkage-reducing agent, Composites Part B Engineering 230 (2022) 109503, https://doi.org/10.1016/j.compositesb.2021.109503.

[24] D. Shen, C. Liu, C. Wen, J. Kang, M. Li, H. Jiang, Restrained cracking failure behavior of concrete containing MgO compound expansive agent under adiabatic condition at early age, Cem. Concr. Compos. 135 (2023) 104825, https://doi.org/10.1016/j.cemconcomp.2022.104825.

[25] S.H. Chu, M. Khan, X. Deng, C. Unluer, Bio-inspired self-prestressing concrete (SPC) involving basalt fibers and expansive agent, Cem. Concr. Res. 155 (2022) 106735, https://doi.org/10.1016/j.cemconres.2022.106735.

[26] S.H. Chu, E.H. Yang, J. Fish, C. Unluer, Bio-inspired strengthening of fiber–matrix interface via ocean-derived MgO expansion agent, Compos. Struct. 377 (2026) 119854, https://doi.org/10.1016/j.compstruct.2025.119854.

[27] K. Aghaee, T. Han, A. Kumar, K.H. Khayat, Mechanism underlying effect of expansive agent and shrinkage reducing admixture on mechanical properties and fiber-matrix bonding of fiber-reinforced mortar, Cem. Concr. Res. 172 (2023) 107247, https://doi.org/10.1016/j.cemconres.2023.107247.

[28] L. Tian, M. Jiao, H. Fu, P. Wang, H. Zhao, W. Zuo, Effect of magnesia expansion agent with different activity on mechanical property, autogenous shrinkage and durability of concrete, Constr. Build. Mater. 335 (2022) 127506, https://doi.org/10.1016/j.conbuildmat.2022.127506.

[29] T. Lv, J. Zhang, C. Li, L. Xu, D. Hou, S. Hong, B. Dong, Durability and sustainable assessment of fly ash-blended cement paste modified by MgO expansive additive, J. Clean. Prod. 468 (2024) 143135, https://doi.org/10.1016/j.jclepro.2024.143135.

[30] J. Luo, Q. Wang, W. Zhou, X. Zhuang, Z. Peng, X. Chang, T. Rabczuk, A coupled phase-field model for sulfate-induced concrete cracking, Int. J. Mech. Sci. 283 (2024) 109694, https://doi.org/10.1016/j.ijmecsci.2024.109694.

[31] N. Cefis, C. Comi, Chemo-mechanical modelling of the external sulfate attack in concrete, Cem. Concr. Res. 93 (2017) 57–70, https://doi.org/10.1016/j.cemconres.2016.12.003.

[32] X. Wu, J. He, J. Tian, Y. Zheng, H. Fu, J. Yuan, S. Lu, W. Huang, Degradation behaviors and damage model of the interface between ECC and concrete under sulfate wet-dry cycling, Constr. Build. Mater. 476 (2025) 141283, https://doi.org/10.1016/j.conbuildmat.2025.141283.

[33] GB 50119-2013, Code for concrete admixture application, China Architecture & Building Press, Beijing, 2013.
[34] GB/T 50082-2009, Standard for test methods of long-term performance and durability of ordinary concrete, China Architecture & Building Press (CABP), Beijing, 2009.
[35] L. Gan, J. Wu, Z. Shen, X. Feng, Deterioration law of basalt fiber reinforced concrete under sulfate attack and dry-wet cycle, China Civil. Eng. J. 54 (11) (2021) 37–46, https://doi.org/10.15951/j.tmgcxb.2021.11.001.
[36] L. Gan, X. Feng, Z. Shen, G. Zheng, Strength evolution model of basalt fiber reinforced concrete under dry-wet cycles of sulfate solutions, J. Southeast Univ. (Nat. Sci. Ed.) 52 (4) (2022) 720–729, https://doi.org/10.3969/j.issn.1001-0505.2022.04.013.
[37] GB/T 50081-2019, Standard for test methods of concrete physical and mechanical properties, China Architecture & Building Press, Beijing, 2019.
[38] GB/T 50476-2019, Standard for design of concrete structure durability, China Architecture & Building Press, Beijing, 2019.
[39] GB/T 11899-1989 Water quality–Determination of sulfate–Gravimetric method, China Architecture & Building Press, Beijing, 1989.
[40] Z. Wang, L. Jin, T. Fan, T. Wu, A meso-scale simulation method for mechanical response of recycled aggregate concrete under external sulfate attack considering diffusion-chemo-expansion-mechanics coupling, Mater. Chem. Phys. 351 (2026) 132005, https://doi.org/10.1016/j.matchemphys.2025.132005.
[41] J. Li, F. Xie, G. Zhao, L. Li, Experimental and numerical investigation of cast-in-situ concrete under external sulfate attack and drying-wetting cycles, Constr. Build. Mater. 249 (2020) 118789, https://doi.org/10.1016/j.conbuildmat.2020.118789.
[42] X. Zhu, M. Zhang, X. Wang, Y. Zhang, Study on sulfate corrosion life prediction model of manufactured sand concrete based on multi-field coupling mechanism, J. Build. Eng. 115 (2025) 114565, https://doi.org/10.1016/j.jobe.2025.114565.
[43] R. Bai, S. Liu, L. Yin, C. Yan, J. Zhou, L. Lu, L. Li, Freeze-thaw damage assessment of engineered cementitious composites using the electrochemical impedance spectroscopy method, Mater. Des. 230 (2023) 111965, https://doi.org/10.1016/j.matdes.2023.111965.
[44] J. Tang, L. Zhang, S. Lu, J. Liu, S. Wang, S. Li, J. Li, Z. Li, Effects of calcium carbide slag incorporation on the multiscale performance of sulfoaluminate cement mortars, Materials 19 (4) (2026) 746, https://doi.org/10.3390/ma19040746.
[45] S. Lu, S. Liu, L. Yin, C. Yan, H. Wang, D. Yin, S. Liu, L. Li, Evolution characteristics of engineered cementitious composite pore structure and its correlation with the tensile property under simulated traffic vibrations at an early age, J. Mater. Sci. 59 (2) (2024) 491–518, https://doi.org/10.1007/s10853-023-09222-8.
[46] D. Zou, M. Zhang, S. Qin, X. Zhang, T. Liu, Mechanistic insights into two-stage expansion of concrete under external sulfate attack, Constr. Build. Mater. 446 (2024) 138027, https://doi.org/10.1016/j.conbuildmat.2024.138027.
[47] S. Xu, K. Yan, T. Jiang, Y. Wang, S. Shi, W. Li, Y. Zhao, K. Sun, J. Yu, X. Wu, Compressive Properties of Basalt Fibers and Polypropylene Fiber-Reinforced Lightweight Concrete, Acs Omega 9 (25) (2024) 26973–26982, https://doi.org/10.1021/acsomega.3c10076.
[48] P. Smarzewski, Influence of basalt-polypropylene fibres on fracture properties of high performance concrete, Compos. Struct. 209 (2019) 23–33, https://doi.org/10.1016/j.compstruct.2018.10.070.
[49] L. Mo, M. Deng, M. Tang, A. Al-Tabbaa, MgO expansive cement and concrete in China: Past, present and future, Cem. Concr. Res. 57 (2014) 1–12, https://doi.org/10.1016/j.cemconres.2013.12.007.
[50] V. Corinaldesi, A. Nardinocchi, Mechanical characterization of Engineered Cement-based Composites prepared with hybrid fibres and expansive agent, Compos. Part B Eng. 98 (2016) 389–396, https://doi.org/10.1016/j.compositesb.2016.05.051.
[51] W. Xue, X. Peng, M.S. Alam, Z. Wang, H. Wu, J. Lin, Pore structure, mechanical property and permeability of concrete under sulfate attack exposed to freeze–thaw cycles, Arch. Civ. Mech. Eng. 24 (2) (2024) 130, https://doi.org/10.1007/s43452-024-00944-3.
[52] H. Ma, H. Zhu, H. Chen, Y. Ni, X. Xu, Q. Huo, Shrinkage-reducing measures and mechanisms analysis for alkali-activated coal gangue-slag mortar at room temperature, Constr. Build. Mater. 252 (2020) 119001, https://doi.org/10.1016/j.conbuildmat.2020.119001.
[53] D. Ren, D. Shi, X. Wang, Relationship between chloride ion penetration resistance and pore structure of PVA fiber-reinforced concrete with coal gangue as fine aggregate, Constr. Build. Mater. 507 (2026) 145060, https://doi.org/10.1016/j.conbuildmat.2025.145060.
[54] J. Wei, N. Farzadnia, K.H. Khayat, Synergistic effect of macro synthetic fiber and shrinkage-reducing admixture on engineering properties of fiber-reinforced super-workable concrete, Constr. Build. Mater. 414 (2024) 134566, https://doi.org/10.1016/j.conbuildmat.2023.134566.
[55] E.K. Melara, P.O. Trentin, E. Pereira, R.A. Medeiros-Junior, Contribution to the service-life modeling of concrete exposed to sulfate attack by the inclusion of electrical resistivity data, Constr. Build. Mater. 322 (2022) 126490, https://doi.org/10.1016/j.conbuildmat.2022.126490.
[56] G. Yin, X. Zuo, X. Li, Y. Zou, An integrated macro-microscopic model for concrete deterioration under external sulfate attack, Eng. Fract. Mech. 240 (2020) 107345, https://doi.org/10.1016/j.engfracmech.2020.107345.
[57] X. Qu, T. Guo, J. Cai, Y. Hu, B. Huang, T. Xie, Characterization and analysis of electrothermal, thermoelectric, and current discharge properties of alkali-activated materials: implications for energy conversion, Cem. Concr. Compos. 159 (2025) 105987, https://doi.org/10.1016/j.cemconcomp.2025.105987.
[58] G. Li, B. Wang, D.K. Panesar, Q. Chen, Electrochemical impedance spectroscopy: Effects of stray current and sulfate exposure on rubber powder mortar, Cem. Concr. Compos. 152 (2024) 105615, https://doi.org/10.1016/j.cemconcomp.2024.105615.
[59] S. Chang, F. Gao, L. Wang, Q. Jin, S. Liu, L. Wan, Deterioration mechanism of supersulfated cement paste exposed to sulfate attack and combined acid-sulfate attack, Constr. Build. Mater. 414 (2024) 134978, https://doi.org/10.1016/j.conbuildmat.2024.134978.
[60] D. Gao, L. Yang, Y. Pang, Z. Li, Q. Tang, Effects of a novel hydrophobic admixture on the sulfate attack resistance of the mortar in the wet-dry cycling environment, Constr. Build. Mater. 344 (2022) 128148, https://doi.org/10.1016/j.conbuildmat.2022.128148.
[61] X. Ouyang, X. Li, J. Li, Y. Ma, M. Zhang, Z. Li, J. Fu, Multiscale microstructure and reactivity evolution of recycled concrete fines under gas-solid carbonation, Cem. Concr. Compos. 157 (2025) 105903, https://doi.org/10.1016/j.cemconcomp.2024.105903.
[62] R. Bai, C. Yan, J. Zhang, S. Liu, L. Jing, Microstructural characteristics of aluminosilicate minerals in cement clinker prepared from coal gangue, carbide slag, and desulfurization gypsum, Constr. Build. Mater. 451 (2024) 138861, https://doi.org/10.1016/j.conbuildmat.2024.138861.
[63] D. Huang, X. Wang, X. Li, L. Su, J. Tian, Y. Li, Y. Liu, Research on the mechanical properties and pore structure deterioration of Basalt-polyvinyl alcohol hybrid fiber concrete under the coupling effects of sulfate attack and freeze-thaw cycles, Constr. Build. Mater. 473 (2025) 140949, https://doi.org/10.1016/j.conbuildmat.2025.140949.
[64] H. Wang, Y. Li, H. Liao, D. Zou, T. Liu, Deterioration mechanism of OPC mortar under combined chemical and physical sulfate attack in partial immersion, Constr. Build. Mater. 475 (2025) 141187, https://doi.org/10.1016/j.conbuildmat.2025.141187.
[65] M. Ohno, K. Maekawa, Fully coupled physicochemical-mechanical modeling of sulfate attack-induced expansion in cement-based materials, Cem. Concr. Compos. 161 (2025) 106076, https://doi.org/10.1016/j.cemconcomp.2025.106076.
[66] K. Piriyakul, A. Petcherdchoo, K. Punthutaecha, T. Phoo-ngernkham, Unconfined compressive strength and small-strain shear modulus of soft marine clay improved by ordinary Portland cement and polyester fibers with modeling by Michaelis-Menten kinetics, J. Road. Eng. 6 (1) (2026) 134–147, https://doi.org/10.1016/j.jreng.2025.01.007.
[67] W. Zhang, D. Liu, K. Cao, Y. Jin, Y. Tang, Multiscale damage evolution mechanism and failure early-warning model of the ECC-concrete interface under sulfate erosion, Constr. Build. Mater. 520 (2026) 145971, https://doi.org/10.1016/j.conbuildmat.2026.145971.
[68] A. Claude, R. Sinaasappel, J. van de Groep, N. Shahidzadeh, Metastability limit of hydrated phases of sodium sulfate under temperature cycling for heat storage, J. Phys. Chem. C. 130 (10) (2026) 3721–3729, https://doi.org/10.1021/acs.jpcc.5c08083.
[69] R. Wijnhorst, M. Demmenie, E. Jambon-Puillet, F. Ariese, D. Bonn, N. Shahidzadeh, Softness of hydrated salt crystals under deliquescence, Nat. Commun. 14 (1) (2023) 1090, https://doi.org/10.1038/s41467-023-36834-0.
[70] Q. Xiong, L. Tong, J. Huang, J. Yang, Q. Liu, Salt crystallization in porous materials: a quasi-local transport model for evaluating pore filling process, Constr. Build. Mater. 462 (2025) 139904, https://doi.org/10.1016/j.conbuildmat.2025.139904.
[71] L. Caneda-Martínez, W. Kunther, C. Medina, M.I. Sánchez De Rojas, M. Frías, Exploring sulphate resistance of coal mining waste blended cements through experiments and thermodynamic modelling, Cem. Concr. Compos. 121 (2021) 104086, https://doi.org/10.1016/j.cemconcomp.2021.104086.
[72] R. Yan, Experimental Research on Sulfate Attack Resistance of Hybrid Polypropylene Fiber Reinforced Concrete with Different Sizes, in: Chongqing University, Chongqing, 2021.

[73] Z. Xuan, Q. Chun-xiang, C. Huaicheng, L. Chengyao, K. Wence, Calculation of expansion stresses and strains in concrete under sulfate crystallization attack in dry - wet cycles environments, J. Mater. Civ. Eng. 3 (33) (2020) 20479, https://doi.org/10.1061/(ASCE)MT.1943-5533.0003499.
[74] M. Barka, O. Taleb, A.K. Tedjditi, H. Soualhi, A.S. Benosman, M. Mouli, New insights on rheology, durability and mechanical and thermal properties of polyester and steel fiber-reinforced self-compacting concretes, Eur. J. Environ. Civ. Eng. 29 (8) (2025) 1467–1490, https://doi.org/10.1080/19648189.2024.2441970.
[75] Y. Zhao, S. Zhang, Q. Xu, K. Wang, Z. Xu, T. Long, T. Jin, M. Jiang, P. Liu, Synergistic enhancement of mechanical and thermal properties in basalt fiber reinforced composites through nanotube and graphene bridging structure: a multi-scale simulation, Composites Part B Engineering 297 (2025) 112289, https://doi.org/10.1016/j.compositesb.2025.112289.
[76] T. Hua, Z. Cao, S. Zhang, R. Guo, Dual mechanism of CaO-based expansive agent on sulfate attack of marine concrete: Competitive interaction between pore structure and hydration products, Constr. Build. Mater. 487 (2025) 142091, https://doi.org/10.1016/j.conbuildmat.2025.142091.
[77] Q. Zheng, E. Yang, Y. Xu, C. Li, X. Zhu, Z. Zhang, Z. Jiang, Aqueous carbonation-induced self-healing of UHPFRC: role of sulfur/magnesium-rich expansive agents in crack closure and mechanical restoration, Cem. Concr. Res. 203 (2026) 108159, https://doi.org/10.1016/j.cemconres.2026.108159.
[78] D. Yang, C. Yan, S. Liu, J. Zhang, Z. Hu, Stress-strain constitutive model of concrete corroded by saline soil under uniaxial compression, Constr. Build. Mater. 213 (2019) 665–674, https://doi.org/10.1016/j.conbuildmat.2019.03.153.
[79] S. Liu, N. Wang, D. Yin, Y. Li, B. Yan, R. Bai, X. Wang, L. Li, L. Yin, Degradation mechanism and compressive strength prediction of polyvinyl alcohol fiber-engineered cementitious composites under coupled salt corrosion and freeze-thaw cycles, Constr. Build. Mater. 497 (2025) 143879, https://doi.org/10.1016/j.conbuildmat.2025.143879.
[80] S. Qin, D. Zou, T. Liu, A. Jivkov, A chemo-transport-damage model for concrete under external sulfate attack, Cem. Concr. Res. 132 (2020) 106048, https://doi.org/10.1016/j.cemconres.2020.106048.
[81] S. Qin, M. Zhang, D. Zou, T. Liu, A failure thickness prediction model for concrete exposed to external sulfate attack, Constr. Build. Mater. 416 (2024) 135202, https://doi.org/10.1016/j.conbuildmat.2024.135202.
[82] K. Wang, J. Guo, L. Yang, Effect of dry–wet ratio on sulfate transport-reaction mechanism in concrete, Constr. Build. Mater. 302 (2021) 124418, https://doi.org/10.1016/j.conbuildmat.2021.124418.
[83] H. Li, X. Wu, Q. Nie, J. Yu, L. Zhang, Q. Wang, Q. Gao, Lifetime prediction of damaged or cracked concrete structures: A review, Structures 71 (2025) 108095, https://doi.org/10.1016/j.istruc.2024.108095.
[84] M. Zhang, S. Qin, H. Lyu, C. Chen, D. Zou, A. Zhou, Y. Li, T. Liu, A transport-chemical-physical–mechanical model for concrete subjected to external sulfate attack and drying–wetting cycles, Eng. Fract. Mech. 293 (2023) 109726, https://doi.org/10.1016/j.engfracmech.2023.109726.